



CrossEarth-SAR: A SAR-Centric and Billion-Scale Geospatial Foundation Model for Domain Generalizable Semantic Segmentation

Ziqi Ye^{1,2*}, Ziyang Gong^{3*†}, Ning Liao^{3*}, Xiaoxing Hu^{2,3,4}, Di Wang^{5,6}, Hongruixuan Chen⁷, Chen Huang⁸, Yiguo He³, Yuru Jia^{9,10}, Xiaoxing Wang³, Haipeng Wang^{1‡}, Xue Yang^{3‡}, Junchi Yan^{3,2‡}

¹Fudan University, ²Shanghai Innovation Institute, ³Shanghai Jiao Tong University, ⁴Beijing Institute of Technology, ⁵Wuhan University, ⁶Zhongguancun Academy, ⁷The University of Tokyo, ⁸Sun Yat-sen University, ⁹KU Leuven, ¹⁰KTH

*Equal contribution, †Project lead, ‡Corresponding Author

Abstract

Synthetic Aperture Radar (SAR) enables global, all-weather earth observation. However, owing to diverse imaging mechanisms, domain shifts across sensors and regions severely hinder its semantic generalization. To address this, we present CrossEarth-SAR, the first billion-scale SAR vision foundation model built upon a novel physics-guided sparse mixture-of-experts (MoE) architecture incorporating physical descriptors, explicitly designed for cross-domain semantic segmentation. To facilitate large-scale pre-training, we develop CrossEarth-SAR-200K, a weakly and fully supervised dataset that unifies public and private SAR imagery. We also introduce a benchmark suite comprising 22 sub-benchmarks across 8 distinct domain gaps, establishing the first unified standard for domain generalization semantic segmentation on SAR imagery. Extensive experiments demonstrate that CrossEarth-SAR achieves state-of-the-art results on 20 benchmarks, surpassing previous methods by over 10% mIoU on some benchmarks under multi-gap transfer. All code, benchmark and datasets will be publicly available.

Date: March 13, 2026

Project Page: <https://crossearth.cn/>

Code: <https://github.com/VisionXLab/CrossEarth-SAR>

Benchmark Datasets: <https://huggingface.co/datasets/conquer997/CrossEarth-SAR-Benchmarks>

1 Introduction

Synthetic Aperture Radar (SAR) is an indispensable tool for earth observation, prized for its ability to capture high-resolution imagery regardless of weather conditions or time of day. This all-weather, all-day capability is critical for time-sensitive applications, especially in disaster mitigation [16], as well as for long-term environmental monitoring [18] and urban management [30]. At the core of translating complex SAR data into actionable insights lies in semantic segmentation, the task of assigning a class label to every pixel in a captured scene.

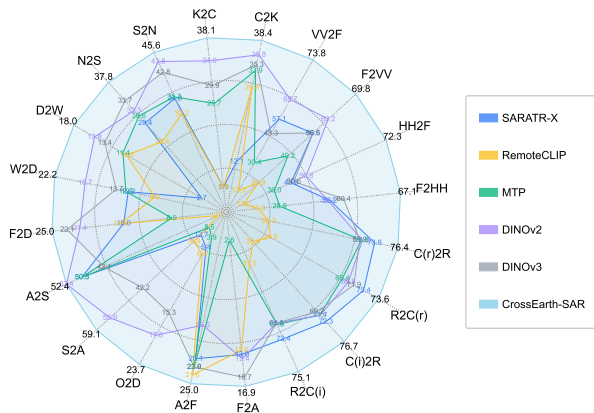


Figure 1 We evaluate representative models on 22 valuation benchmarks, where CrossEarth-SAR achieves SOTA performance (mIoU) on 20 settings across various segmentation scenes, demonstrating strong generalizability.

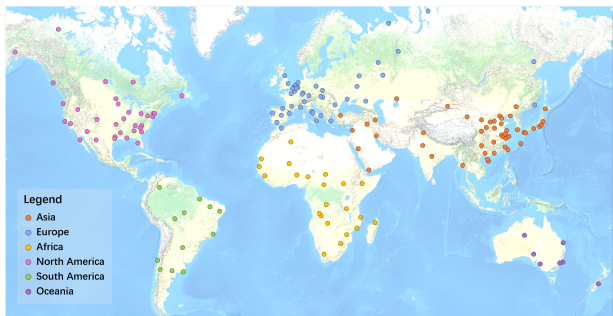


Figure 2 Geographic distribution of the CrossEarth-SAR-200K, demonstrating its comprehensive coverage across hundreds of cities on six continents.

However, achieving robust semantic understanding in SAR is fundamentally more challenging than in the visible spectrum domain. This difficulty stems not only from the unfamiliar appearance of radar images but from three core challenges that directly conflict with the assumptions of modern vision models. First, SAR’s coherent imaging process creates inherent multiplicative speckle, a granular noise that corrupts local feature statistics and textures, severely degrading the performance of models reliant on learned textural patterns [1, 2, 6, 28]. Second, SAR’s side-looking geometry introduces severe spatial distortions, such as layover, foreshortening, and shadow, which drastically alter the apparent shape and topology of objects like buildings and mountains, severely affect models trained on standard geometric priors [19, 56, 62]. Third, SAR measures radar backscatter, not color. This physical measurement, tied to surface roughness and dielectric properties, creates profound semantic ambiguity: dissimilar classes can share identical dark appearances, while a single class can appear vastly different based solely on moisture content or crop row orientation [38, 51].

Beyond these inherent pixel-level and geometric complexities lies the most significant barrier to scalable applications, *i.e.*, the domain specificity of SAR. Different from web images widely used in the vision community, SAR data is not a monolith. Its characteristics are fragmented by a multitude of acquisition parameters, including sensor platform (e.g., Sentinel-1, ALOS-2, Capella), frequency band (C, L, X bands), polarization mode (HH, HV, VH, and VV), and incidence angle. A model trained on data from one sensor, in one region, under one set of conditions, catastrophically fails when applied to another. This extreme domain fragmentation has hindered the development of a truly generalizable and robust SAR understanding model.

In this context, achieving cross-domain generalization is the essential yet largely underexplored challenge for the SAR community [10, 14]. To bridge this gap, we argue that unlocking large-scale generalization requires a massive model capacity to absorb the extreme diversity of SAR data. We introduce **CrossEarth-SAR**, the first **billion-scale** SAR vision foundation model. To make this scale computationally feasible, CrossEarth-SAR is built upon a sparse Mixture-of-Experts (MoE) architecture. This design allows the parameter count to scale into the billions (to capture extreme domain diversity) while maintaining a manageable compute cost per image. Additionally, we also incorporate a novel physics-guided routing mechanism to further stabilize expert selection for SAR’s unique physical properties.

To support the training and rigorous evaluation of such a large-scale model, we introduce two additional resources. First, the CrossEarth-SAR-200K dataset, which integrates 200K supervised images by combining public and privately collected SAR data. Second, a comprehensive benchmark collection encompassing 22 benchmarks across 8 domain gaps, providing the first unified standard for assessing DG in SAR imagery.

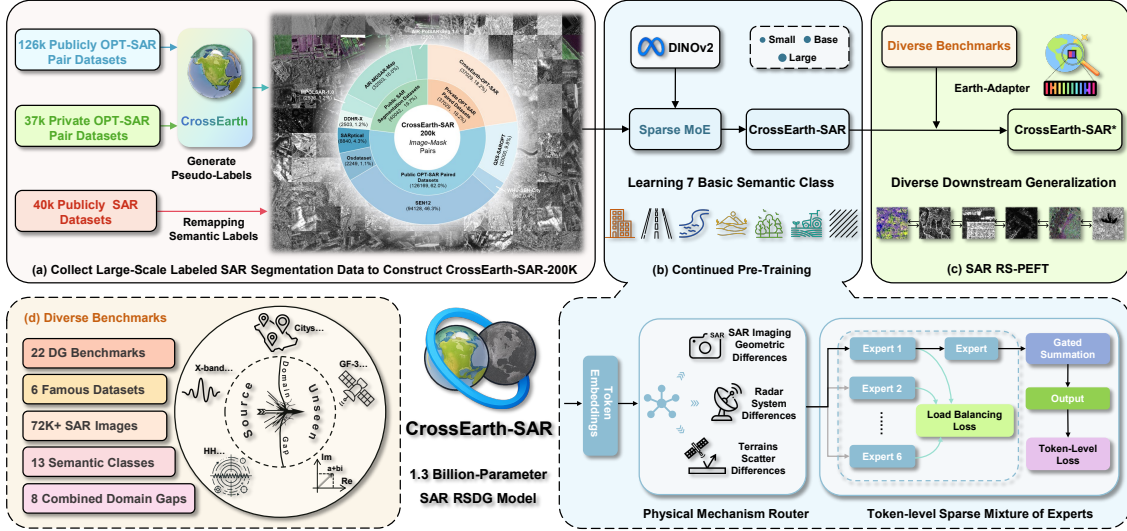


Figure 3 Framework of CrossEarth-SAR. (a) Collect large-scale labeled SAR segmentation data to construct CrossEarth-SAR-200K. (b) The continued pre-training structure of CrossEarth-SAR. (c) SAR RS-PEFT by Earth-Adapter. (d) The information of diverse benchmarks.

Our main contributions are summarized as follows:

- We propose **CrossEarth-SAR**, the first **billion-scale** SAR vision foundation model featuring a physics-guided sparse MoE architecture, specifically optimized for cross-domain semantic segmentation. In addition, we also provide small, base, and large versions of CrossEarth-SAR to support hierarchical application needs.
- We construct **CrossEarth-SAR-200K**, a large-scale semantic segmentation dataset integrating weakly and fully supervised SAR imagery to support global-scale continuous pre-training.
- We curate a standardized benchmark collection encompassing 22 sub-benchmarks across 8 domain gaps, enabling unified evaluation of SAR domain generalization.
- Extensive experiments and analyses show the superiority of CrossEarth-SAR and provide new insights into domain-generalizable SAR representation learning.

2 Related Work

2.1 Cross-Domain Semantic Segmentation in RS

Cross-domain semantic segmentation is a fundamental task for testing model generalization. While notable progress has been made in fields like medicine [11, 33, 34] and autonomous driving [8, 9, 17, 20], the problem remains particularly acute in RS. RS imagery suffers from severe domain gaps caused by differences in sensors, resolution, season, spectral bands, and geographic conditions [36]. Within RS, efforts in the visible spectrum domain have evolved from conventional adversarial alignment and self-training methods [3, 4, 24, 29, 71–73] to the recent adoption of Vision Foundation Models (VFMs) [12, 44, 65, 66]. Notably, CrossEarth [10], the first VFM for domain-generalized segmentation, has set a strong benchmark for optical generalization.

However, in challenging SAR scenarios, achieving generalization remains difficult [31, 39] due to the unique characteristics of SAR imagery, such as speckle noise and complex electromagnetic scattering mechanisms [40, 48, 63]. Existing mainstream methods often rely on paired optical images to support SAR semantic segmentation [41, 52, 57, 64], but their generalization capabilities remain limited to relatively narrow domain gaps. How to fully unlock the potential of VFMs for cross-domain generalization in SAR imagery remains largely underexplored.

2.2 SAR Vision Foundation Models

The development of geospatial foundation models has been largely concentrated on optical and temporal multispectral data. Prominent examples include SatMAE [5], HyperSIGMA [45], SkySense [12], SkySense++ [55] and SkySenseV2 [68]. While powerful in their domain, their architectures and pre-training strategies do not address the unique backscattering physics and noise characteristics of SAR. Recently, VFMs focusing on SAR have emerged. A significant portion of these efforts centers on object-level applications, such as object detection [25] or automatic target recognition [22]. These models are optimized for sparse object localization, which does not directly address dense, pixel-level semantic segmentation. Other efforts are geared towards learning general-purpose representations [21, 47]. While they show promise, they are not designed for cross-domain generalization. Thus, a large-scale VFM that is built to achieve robust domain-generalizable semantic segmentation in SAR remains a critical missing piece.

3 Method

3.1 Overview

The architecture of CrossEarth-SAR is a physics-guided sparse MoE integrated into a DINOv2 backbone f_ϕ . The backbone follows the standard ViT stacking. In each block, the original Feed-Forward Network (FFN) is replaced by a MoE composed of a router R_ψ and n experts $\{E_k\}_{k=1}^n$, which are initialized from the DINOv2 FFN weights.

At each training iteration, an input SAR image is first copied to 3-channel $X \in \mathbb{R}^{3 \times H \times W}$ and forwarded through f_ϕ . In parallel, three SAR physics descriptors $s \in \mathbb{R}^3$ are computed. For each ViT block, the token embeddings produced by attention are augmented with s and passed to the router R_ψ to activate an expert. A load-balancing constraint \mathcal{L}_{BC} is applied during the routing process.

After propagating through all blocks, the final embeddings are decoded by a Mask2Former f_θ to generate the prediction \hat{Y} . During training, the parameters of f_ϕ , R_ψ , $\{E_k\}_{k=1}^n$, and f_θ are jointly optimized using the segmentation objective \mathcal{L}_{seg} together with \mathcal{L}_{BC} . In the following, we illustrate the details and motivations of the components in CrossEarth-SAR.

3.2 SAR Physical Descriptor

A critical challenge in applying sparse MoE architectures to SAR is ‘Routing Instability’. Standard routers select experts based on learned token embeddings. However, these embeddings fluctuate dramatically when processing heterogeneous SAR data due to severe physical domain shifts. This prevents the router from consistently activating the appropriate expert for a given domain, undermining the MoE’s specialization objective.

To mitigate this issue, CrossEarth-SAR introduces a SAR Physical Operator $g_{sar}(\cdot)$ to compute three representative descriptors for each input image. These descriptors provide stable, physically grounded cues that complement token embeddings and supply physics-aware guidance to the router, enabling more consistent expert activation.

Notably, before calculation, we transform all input X to a log-intensity representation X' for numerical stability by

$$X' = \log(1 + |X|). \quad (1)$$

Next, we will illustrate the details of three descriptors.

Imaging Geometry. SAR image appearance is sensitive to imaging geometry. Changes in sensor position or viewing angle alter object shapes and edge orientations, causing inconsistent features of the same target across domains. To quantify this difference, we introduce the Directional Entropy H_{DE} , which evaluates the structural regularity of an image by analyzing the distribution of gradient directions in X' . Given the Sobel gradients (g_x, g_y) , we first compute the gradient direction for each pixel:

$$\theta = \text{atan2}(g_y, g_x). \quad (2)$$

These direction angles are then quantized into N discrete bins to form a histogram of gradient orientations. Finally, the entropy of this histogram is computed as:

$$H_{DE} = - \sum_{i=1}^N p_i \ln p_i, \quad (3)$$

where (p_i) denotes the normalized proportion of pixels whose gradient direction falls into the i -th bin.

A low H_{DE} indicates that image gradients are concentrated in a dominant direction, typically corresponding to clear linear or edge-like structures. A high value suggests that gradient directions are more evenly distributed and the scene contains richer, more irregular structural patterns.

Radar System. Variations in radar parameters, such as frequency band and polarization, lead to distinct speckle statistics across sensors, introducing inconsistent noise levels that challenge generalization. To capture speckle variations induced by the system imaging mechanism, we use the Equivalent Number of Looks (ENL), a widely adopted measure of speckle strength in SAR imaging. ENL is defined as:

$$\text{ENL} = \left(\frac{\mu}{\sigma} \right)^2, \quad (4)$$

where μ and (σ) are the mean and standard deviation of the X' . A higher ENL indicates more stable intensity statistics and weaker speckle, while a lower ENL reflects stronger noise fluctuations. This scalar provides a simple and reliable way to compare system-level noise properties across different SAR sources.

Object Scattering. Surface scattering varies with material roughness and dielectric properties, resulting in diverse texture patterns that differ significantly across domains and hinder consistent feature generalization. To capture this texture variability, we compute a Local Roughness descriptor by applying spatial averaging to X' and measuring the variance among blockwise mean values:

$$R_{\text{LR}} = \text{Var}(\mu_j)_{j=1}^M, \quad (5)$$

where M is the total number of spatial blocks obtained from average pooling. Each blockwise mean μ_j is defined as:

$$\mu_j = \frac{1}{|B_j|} \sum_{(u,v) \in B_j} X'(u,v), \quad (6)$$

where (B_j) denotes the set of pixels within the j -th local block of X' . Consequently, a higher R_{LR} value implies large variations in brightness across regions, corresponding to a scene composed of complex texture. Conversely, a lower value indicates a smooth texture.

Finally, the three physical descriptors are concatenated to form a 3D tensor:

$$s = [H_{DE}, \text{ENL}, R_{\text{LR}}] \in \mathbb{R}^3. \quad (7)$$

Ablation studies (see Tab. 5, Section 5.5) demonstrate that incorporating these physical quantities guides the model to focus on the inter-domain physical features of SAR images, effectively improving its domain generalization capability and downstream segmentation performance.

3.3 Physics-Guided Sparse MoE

To model the inherent multi-source variability of SAR imagery, we try to curate a model with sufficient capacity to capture its diverse and complex imaging mechanisms. However, simply enlarging a dense network leads to prohibitive computational costs. The sparse MoE architecture provides a principled solution: its multi-expert design allows different experts to specialize in different SAR characteristics, while sparse activation ensures that the inference cost remains comparable to a standard FFN. Motivated by this, we design physics-guided Sparse MoE.

Table 1 CrossEarthSAR benchmark collection. North/South: northern/southern China. KR/CN: Korea/China. VV/HH: single-polarization. Full: full-polarization. Complex(r)/Complex(i): real or imaginary part of complex-valued PolSAR data.

Domain Gap	Dataset	Source Domain	Target Domain	Abbreviation	Train	Test	Categories
Unseen Region	AIR-PolSAR-Seg 2.0 [70]	North	South	N2S	600	159	5
		South	North	S2N	633	150	5
	DDHR-SK [37]	KR	CN	K2C	4916	1566	6
		CN	KR	C2K	6265	1229	6
Unseen Polarization	AIR-PolSAR-Seg 2.0 [70]	VV	Full	VV2F			6
		Full	VV	F2VV	1233	309	6
		HH	Full	HH2F			6
		Full	HH	F2HH			6
Unseen Complex Values	AIR-PolSAR-Seg 2.0 [70]	Complex(r)	Real	C(r)2R			6
		Real	Complex(r)	R2C(r)	1233	309	6
		Complex(i)	Real	C(i)2R			6
		Real	Complex(i)	R2C(i)			6
Unseen Region and Polarization	FUSAR-Map [41]	FUSAR	AIR	F2A	1952	309	5
	AIR-PolSAR-Seg 2.0 [70]	AIR	FUSAR	A2F	1233	488	5
Unseen Region and Platform	OpenEarthMap [57]	OpenEarthMap	DDHR	O2D	13865	1567	6
	DDHR-SK [37]	DDHR	OpenEarthMap	D2O	6265	3467	6
Unseen Region and Microwave Band	SARBuD [54]	SARBuD	AIR	S2A	20000	309	1
	AIR-PolSAR-Seg 2.0 [70]	AIR	SARBuD	A2S	1233	5000	1
Unseen Region, Polarization and Microwave Band	DDHR-SK [37]	DDHR	FUSAR	D2F	6265	488	5
	FUSAR-Map [41]	FUSAR	DDHR	F2D	1952	1566	5
Unseen Region, Platform and Microwave Band	WHU-OPT-SAR [23]	WHU-SAR	DDHR	W2D	7040	1567	6
	DDHR-DK [37]	DDHR	WHU-SAR	D2W	6265	1760	6

Router. Given the token embeddings $Z \in \mathbb{R}^{B \times N \times C}$ and the descriptors s . We tile s across tokens to get $S \in \mathbb{R}^{B \times N \times 3}$. The router computes a score over n experts and selects the top- k candidates for each token:

$$\pi = \text{softmax}(W_r[Z \| S] + b_r), \quad (8)$$

where $[\cdot]$ means the concat and $\pi \in \mathbb{R}^{B \times N \times n}$ denotes the expert scores.

Token-Level MoE. For each token embedding $z \in \mathbb{R}^C$, the router selects the top- k experts according to scores $\pi \in \mathbb{R}^n$. Let \mathcal{I} denote the set of selected expert indices; the gating weights are normalized as:

$$g_k = \frac{\pi_k}{\sum_{m \in \mathcal{I}} \pi_m}, \quad k \in \mathcal{I}, \quad (9)$$

and the final output is the sparse aggregation, defined as:

$$\tilde{z} = \sum_{k \in \mathcal{I}} g_k \cdot E_k(z). \quad (10)$$

This design preserves computational efficiency comparable to the original FFN while allowing dynamic specialization across SAR imaging conditions.

Training Objective. To prevent expert collapse, we impose a load-balancing loss. Let f_k be the fraction of tokens assigned to expert k and p_k the mean routing probability. The balancing loss is as follows:

$$\mathcal{L}_{BC} = \lambda_{BC} n \sum_{k=1}^n f_k p_k, \quad (11)$$

where λ_{BC} is the weight set to 0.005. The complete training objective combines segmentation and balancing terms:

$$\mathcal{L} = \mathcal{L}_{\text{seg}} + \mathcal{L}_{BC}. \quad (12)$$

4 CrossEarth-SAR-200K & Benchmark

4.1 CrossEarth-SAR-200K

CrossEarth-SAR-200K consists of publicly available SAR images with real labels and collected SAR images with pseudo labels, as shown in Figure 3(a).

For data without semantic segmentation labels, the strongest RSDG model CrossEarth, is adopted to segment the optical images paired with SAR images. The R2U weights trained on 7 classes from the LoveDA dataset are used. The resulting predictions are assigned as labels for the corresponding SAR images. This pseudo-labeling pipeline follows a widely accepted practice in SAR-related semantic segmentation, and has been adopted by several representative benchmarks, such as DDHR [37], FUSAR-Map [41], WHU-OPT-SAR [23], and OpenEarthMap-SAR [57]. Additionally, to estimate label confidence, we apply four models (SatMAE [5], ScaleMAE [35], MTP [44], and CrossEarth [10]) to predict pseudo labels on 1K samples. The mean agreement [57] across these models reaches 75.88%, exceeding the 63.20% computed on OpenEarthMap-SAR [57], which supports the reliability of the generated labels.

For the continuous pre-training stage, CrossEarth-SAR-200K-Val is a 4k-image split sampled from CrossEarth-SAR-200K with ground-truth labels, and is used for validation. As part of preprocessing, all SAR images are cropped or resized to 512×512. More details on the composition and structure of CrossEarth-SAR-200K are provided in Fig. 2, Fig. 3(a). All CrossEarth-SAR-200K, including our collected dataset, will be fully available.

4.2 Benchmark

For fair evaluation of generalizability of existing models in SAR modality, we curate 22 benchmarks based on 6 widely-used SAR RS semantic segmentation datasets including AIR-PolSAR-Seg-2.0 [70], DDHR-SK [37], FUSAR-Map [41], OpenEarthMap-SAR [57], SARBuD [54], and WHU-OPT-SAR [23], and extend them to DG settings, as shown in Tab. 1. Our benchmark comprises 22 different tasks across 8 compositional domain gaps: (1) Unseen Region; (2) Unseen Polarization; (3) Unseen Complex Number; (4) Unseen Region and Polarization; (5) Unseen Region and Platform; (6) Unseen Region and Microwave Band; (7) Unseen Region, Polarization and Microwave Band; (8) Unseen Region, Platform and Microwave Band. The benchmark datasets are non-overlapping with CrossEarth-SAR-200K, and we confirm that there is no data leakage across datasets.

5 Experiments

5.1 Preliminary

We perform continuous pre-training (CPT) on DINOv2 using the CrossEarth-SAR-200K, where all backbone and decoder parameters are trainable. CPT runs for 18 epochs with a batch size of 4, optimized by AdamW [27] with a learning rate of 3e-5. For the CPT stage, we use CrossEarth-SAR-200K-Val as the validation set. All experiments during the CPT stage are conducted in PyTorch using 16 NVIDIA A100 (80 GB) GPUs.

After CPT, we fine-tune CrossEarth-SAR on the source domain and evaluate on unseen target domains. During downstream tasks, all models’ backbones are frozen and only the decoder is trained for 40k iterations with a batch size of 2 on a single NVIDIA 4090 (48 GB) GPU, using a learning rate of 1e-4.

5.2 Generalization across One Gap

In this section, the region, polarization, and complex values are the primary gaps between the source and unseen domains, and there is only one gap in each experiment. Results are presented in Tab. 2. For instance, CrossEarth-SAR-L achieves the best performance on four benchmarks of the common unseen regions in RS. Next, we mainly discuss the unseen polarization and complex-valued gaps, which are unique to SAR imagery.

Different polarization channels interact with terrain through distinct scattering mechanisms, thereby shaping the contrast and class separability in SAR imagery. To probe the generalizability of models when cross-

Table 2 Performance comparison across one-domain-gap benchmarks. All models are frozen during downstream fine-tuning. **Bold** and underlined denote the best and second-best results. Performances in (·) show changes relative to Baseline. * mark means the use of Earth-Adapter for PEFT. Parameters in (·) mean the activated parameters, representing the efficient inference cost of CrossEarth-SAR.

Method	Backbone	Param.	Unseen Region				Unseen Polarization				Unseen Complex Value				Avg.
			N2S	S2N	K2C	C2K	VV2F	F2VV	HH2F	F2HH	C(r)2R	R2C(r)	C(i)2R	R2C(i)	
S12-MoCo [43]	ViT-S [7]	20M	23.2	24.0	8.9	18.6	21.9	16.1	19.8	29.9	29.9	48.1	29.3	37.7	25.6
S12-DINO [43]	ViT-S [7]	20M	22.5	27.0	12.6	30.8	23.0	37.5	15.7	35.1	25.0	59.0	23.4	55.0	30.5
S12-MAE [43]	ViT-S [7]	20M	22.9	29.9	5.9	34.8	12.8	17.7	12.6	15.6	23.7	33.3	19.5	22.8	21.0
DOFA [60]	ViT-B [7]	80M	25.3	27.5	15.8	31.9	20.4	30.7	21.6	30.6	24.6	42.6	24.7	26.3	26.8
SatMAE [5]	ViT-L [7]	300M	26.2	32.1	14.5	33.4	22.5	33.4	17.1	30.0	46.4	34.4	43.4	35.6	30.7
ScaleMAE [35]	ViT-L [7]	300M	26.4	27.2	12.9	30.5	15.1	33.3	14.9	20.2	36.8	40.6	50.0	30.6	28.2
RemoteCLIP [26]	ViT-L [7]	300M	22.4	30.2	5.9	29.8	13.3	20.9	13.0	17.3	22.3	24.9	20.6	31.0	21.0
MTP [44]	ViT-L [7]	300M	30.6	35.3	25.7	33.9	30.4	40.2	36.0	28.9	70.8	65.4	71.4	67.6	44.7
DINOV2 (Baseline) [32]	ViT-L [7]	300M	32.3	43.8	34.0	35.8	65.7	63.2	56.8	55.2	71.3	68.8	71.7	66.8	55.5
DINOV3 [42]	ViT-L [7]	300M	33.7	42.8	29.9	35.3	48.3	56.6	50.6	60.4	69.9	71.9	69.2	66.8	53.0
SARATR-X [13]	HiViT-B [67]	60M	28.4	34.8	5.9	12.1	57.1	56.5	48.6	56.2	73.8	73.4	72.3	72.4	49.3
CrossEarth-SAR-S	ViT-S [7]	90M	34.6	43.2	35.4	35.6	71.3	68.0	68.5	65.0	74.5	73.6	74.2	72.9	59.7
		(20M)	(+2.3)	(-0.6)	(+1.4)	(-0.2)	(+5.6)	(+4.8)	(+11.7)	(+9.8)	(+3.2)	(+4.8)	(+2.5)	(+6.1)	(+4.2)
CrossEarth-SAR-B	ViT-B [7]	300M	36.7	43.4	37.7	37.1	73.5	68.2	70.6	66.5	76.1	74.5	75.1	73.5	61.1
		(80M)	(+4.4)	(-0.4)	(+3.7)	(+1.3)	(+7.8)	(+5.0)	(+13.8)	(+11.3)	(+4.8)	(+5.7)	(+3.4)	(+6.7)	(+5.6)
CrossEarth-SAR-L	ViT-L [7]	1.3B	37.8	45.6	38.1	38.4	73.8	69.8	72.3	67.1	76.4	73.6	76.4	73.6	61.9
		(300M)	(+5.5)	(+1.8)	(+4.1)	(+2.6)	(+8.1)	(+6.6)	(+15.5)	(+11.9)	(+5.1)	(+4.8)	(+4.7)	(+6.8)	(+6.4)
CrossEarth-SAR-L*	ViT-L [7]	1.3B	38.0	46.7	39.1	38.6	73.9	72.2	<u>71.8</u>	68.6	76.9	75.2	76.7	75.1	62.7
		(300M)	(+5.7)	(+2.9)	(+5.1)	(+2.8)	(+8.2)	(+9.0)	(+15.0)	(+13.4)	(+5.6)	(+6.4)	(+5.0)	(+8.3)	(+7.2)

polarization, we conduct experiments on unseen polarization across 4 DG benchmarks: VV2F, F2VV, HH2F, and F2HH. For single to full polarization benchmarks (VV2F and HH2F), CrossEarth-SAR achieves substantial improvements over the baseline. On VV2F, CrossEarth-SAR-L achieves 73.8% mIoU (+8.4%), while on HH2F, CrossEarth-SAR-L reaches 72.3% mIoU (+15.5%). For full to single polarization benchmarks (F2VV and F2HH), CrossEarth-SAR-L also shows remarkable improvements with +6.6% on F2VV and +11.9% on F2HH. Notably, compared with 300M DINOv2 and v3, 90M CrossEarth-SAR-S also shows its superiority with 11.7% improvement in HH2F.

In addition to polarization, SAR inherently produces coherent measurements represented as complex-valued signals. However, most public SAR products only provide real-valued intensity images, which limits the investigation of generalization under complex-valued shifts. To address this, we evaluate generalization across complex-to-real and real-to-complex settings in the one-gap scenario. For complex to real benchmarks (C(r)2R and C(i)2R), CrossEarth-SAR significantly outperforms the baseline across all scales. For example, CrossEarth-SAR-L achieves 76.4% (+5.1%) on C(r)2R and 73.6% (+4.8%) on R2C(r). The similar trends are also shown in benchmarks (C(i)2R and R2C(i)). This indicates that CrossEarth-SAR excels in understanding the complex values of SAR images. Moreover, the improved performance of CrossEarth-SAR-L* highlights the further potential of PEFT.

These results demonstrate that CrossEarth-SAR achieves optimal generalization performance across all one-gap DG benchmarks. The qualitative results for the one-gap setting are provided in the first three rows of Fig. 4.

5.3 Generalization across Two Gaps

Experiments in this section primarily demonstrate the results of two DG gaps, which are formed by pairwise combinations of region, polarization, platform, and microwave band. Notably, the D2O and O2D benchmarks assess global generalization capabilities, while the S2A and A2S benchmarks evaluate building extraction capabilities.

In experiments across two gaps of unseen region and polarization shown in Tab. 3, CrossEarth-SAR achieves the best mIoU on both F2A and A2F benchmarks. Furthermore, CrossEarth-SAR-L delivers performance at 25.0%, surpassing baseline by 9.5% and DINOv3 (second-best) by 1.1% on the A2F benchmark. Similar in experiments across region and platform, CrossEarth-SAR-L* exhibits global generalizability on O2D and D2O benchmarks, surpassing the baseline with 5.3% and 1.2% improvements, respectively. Although the base and

Table 3 Performance comparison on benchmarks across two and three domain gaps. Results show that CrossEarth-SAR-S outperforms other larger FMs. CrossEarth-SAR-L* performance also demonstrates further improvement potential in PEFT of CrossEarth-SAR.

Method	Backbone	Param.	Unseen Region and Polarization		Unseen Region and Platform		Unseen Region and MW Band		Unseen Region and Pol, MW Band		Unseen Region and Platform, MW Band		Avg.
			F2A	A2F	O2D	D2O	S2A	A2S	D2F	F2D	W2D	D2W	
S12-MoCo [43]	ViT-S [7]	20M	7.4	14.7	5.5	8.1	45.2	42.2	6.7	17.4	10.3	5.2	16.3
S12-DINO [43]	ViT-S [7]	20M	8.9	23.6	4.3	9.5	53.9	51.1	15.5	15.9	13.6	10.1	20.6
S12-MAE [43]	ViT-S [7]	20M	12.1	11.4	5.3	8.8	31.3	51.8	19.6	16.1	11.9	14.8	18.3
DOFA [60]	ViT-B [7]	80M	10.3	22.3	4.8	10.2	50.9	27.5	8.3	16.0	12.3	12.5	17.5
SatMAE [5]	ViT-L [7]	300M	11.8	13.1	12.1	9.9	49.2	48.1	20.3	17.5	10.2	7.7	20.0
ScaleMAE [35]	ViT-L [7]	300M	2.4	8.6	9.9	8.2	42.9	47.7	18.6	16.3	7.4	5.3	16.7
RemoteCLIP [26]	ViT-L [7]	300M	12.6	21.6	6.4	10.7	16.4	2.7	21.7	15.5	8.9	11.0	12.8
MTP [44]	ViT-L [7]	300M	2.6	22.0	3.9	4.1	8.5	50.5	7.1	8.0	12.5	11.4	13.1
DINOv2 (Baseline) [32]	ViT-L [7]	300M	13.4	15.5	17.8	10.1	55.9	52.4	26.0	21.4	16.7	13.8	24.3
DINOv3 [42]	ViT-L [7]	300M	15.7	23.9	15.3	8.8	42.2	42.1	22.1	19.5	13.7	13.4	21.7
SARATR-X [13]	HiViT-B [67]	60M	13.0	20.1	5.4	4.4	12.7	50.3	21.7	15.0	12.2	2.7	15.8
CrossEarth-SAR-S	ViT-S [7]	90M	14.1	21.3	19.0	10.7	53.1	50.5	22.6	21.7	16.1	18.9	24.8
		(20M)	(+0.7)	(+5.8)	(+1.2)	(+0.6)	(-2.8)	(-1.9)	(-3.4)	(+0.3)	(-0.6)	(+5.1)	(+0.5)
CrossEarth-SAR-B	ViT-B [7]	300M	15.2	24.2	20.0	9.4	57.1	48.4	21.2	23.2	20.0	15.3	25.4
		(80M)	(+1.8)	(+8.7)	(+2.2)	(-0.7)	(+1.2)	(-4.0)	(-4.8)	(+1.8)	(+3.3)	(+1.5)	(+1.1)
CrossEarth-SAR-L	ViT-L [7]	1.3B	16.9	25.0	23.7	9.6	59.1	52.4	25.1	25.0	22.2	18.0	27.7
		(300M)	(+3.5)	(+9.5)	(+5.9)	(-0.5)	(+3.2)	(+0.0)	(-0.9)	(+3.6)	(+5.5)	(+4.2)	(+3.4)
CrossEarth-SAR-L*	ViT-L [7]	1.3B	16.1	27.0	23.1	11.3	57.9	53.5	26.5	24.1	25.6	19.4	28.5
		(300M)	(+2.7)	(+11.5)	(+5.3)	(+1.2)	(+2.0)	(+1.1)	(+0.5)	(+2.7)	(+8.9)	(+5.6)	(+4.2)

large variants of CrossEarth-SAR on D2O do not surpass the baseline (-0.7% and -0.5%), they outperform DINOv3 by 0.6% and 0.8%, and exceed the SAR foundation model SARATR-X by 5.0% and 5.2%.

In addition to the above, how accurately models perform in the building extraction task also serves as a key indicator of their generalizability. Thus, we conduct experiments on the S2A and A2S benchmarks. Our strongest model, CrossEarth-SAR-L*, achieves improvements of 2.0% and 1.1% mIoU over the baseline on S2A and A2S, respectively. These results indicate that even under two distinct domain gaps, the CrossEarth-SAR maintains a clear advantage in building extraction. The qualitative results for the two-gap setting are provided in the fourth and fifth rows of Fig. 4.

5.4 Generalization across Three Gaps

In this section, we thoroughly investigate the three-gap case, which exemplifies one of the most complex challenges in DG scenarios. There are a total of 4 benchmarks shown in Tab. 3. Excluding the D2F benchmark, CrossEarth-SAR demonstrates remarkable improvements in mIoU across the other three benchmarks: F2D, D2W, and W2D, highlighting its superior performance.

Specifically, CrossEarth-SAR-L* outperforms the baseline by 0.5% and 2.7% mIoU on the D2F and F2D benchmarks, respectively. Although CrossEarth-SAR-L does not surpass the baseline on the D2F benchmark (-0.9%), it both outperform DINOv3 by 3.0% and SARATR-X by 3.4%. Extensive experiments validate CrossEarth-SAR’s exceptional ability to learn domain-invariant representations under diverse and complex SAR domains.

5.5 Ablation Study

As mentioned earlier, we use CrossEarth-SAR-200K-Val for the ablation study during the CPT stage, as summarized in Tab. 5. Specifically, the training paradigm, MoE design, and learning rate ablations are performed on CrossEarth-SAR-L, with Top- $k=1$ and Expert Number $n=6$, as this configuration yields the best overall performance. Additionally, experiments, except for data construction, utilize all CrossEarth-SAR-200K data.

Pseudo-label quality. We first compare training on only fully supervised samples against CrossEarth-SAR-200K, as reported in Tab. 5. Specifically, the latter achieves 59.4% mIoU, surpassing the only 40K setting by a significant 14.3%, showing that extra pseudo labels generated by CrossEarth improve the SAR representation

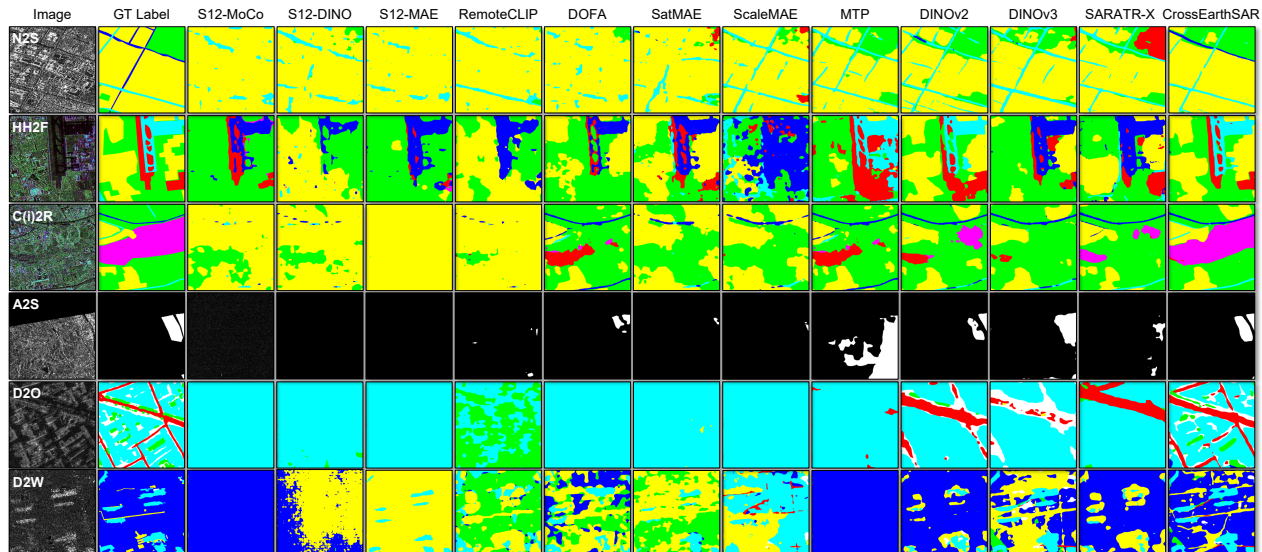


Figure 4 Visualizations of predicted segmentation maps on six representative benchmarks. For the top three rows color map, blue is water, green is vegetation, red is ground, cyan is road, yellow is building, and purple is mountain. For the bottom two rows color map, blue is farmland, green is greenery, red is road, cyan is building, yellow is water, and white is background.

Table 4 Ablation Study on the Structure and Data Validity of CrossEarth-SAR.

Method with CPT dataset	N2S	VV2F	C(r)2R	A2F	O2D	S2A	D2F	W2D	avg.
DINOv2 + 40K real label datasets	32.7	68.6	67.7	16.3	16.1	52.9	20.4	17.1	36.5
DINOv2 + 40K pseudo label datasets (randomly selected)	33.2	66.3	66.9	18.6	17.2	53.6	21.3	17.6	36.8
DINOv2 + CrossEarth-SAR- 200K	36.6	70.6	74.5	23.4	19.7	55.2	21.9	18.9	40.1
CrossEarth-SAR	37.8	73.8	76.4	25.0	23.7	59.1	25.1	22.2	42.9

learning. Additionally, the ablation results in Tab. 4 validate the utility of the pseudo labels. Notably, ground-truth annotations are often constrained to limited geographic regions, whereas pseudo-labeled data are collected at a global scale. The results show that using 40K pseudo-labeled samples yields larger improvements on downstream tasks than using 40K real labels. Moreover, Rows 1 and 3 of Tab. 4 show that adding pseudo labels to real-label training yields an average +3.6% gain on OOD downstream tasks.

Train Paradigm. We evaluate two training paradigms as in Tab. 5, CPT and PEFT, and observe consistent gains: CPT reaches 62.1% mIoU (+2.7%), and CPT+PEFT further improves to 62.4% mIoU (+3.0%), in line with the downstream results in Tab. 2 and 3. Besides, the learning rate is also important, though it does not show strong sensitivity.

MoE Design. For the MoE design in Tab. 5, we start from a plain MoE setup without any additional constraints or priors, which improves performance from DINOv2 to 61.1 mIoU (+1.7%). Introducing \mathcal{L}_{BC} further enhances expert utilization and raises the result to 62.2% mIoU (+2.8%). Incorporating physics descriptors S also brings improvement to 61.6% mIoU (+2.2%), and combining both components achieves the best performance of 62.4% mIoU (+3.0%).

Experts Activation. We ablate the expert number n and Top- k activation. As shown in Tab. 5, with Top- $k=1$, increasing n from 3 to 6 improves mIoU from 60.9% to 62.4%, suggesting that more experts better capture heterogeneous SAR. However, with $n=6$, raising Top- k to 2 or 3 reduces mIoU (62.4% \rightarrow 61.3%), likely because 200K samples favor single-expert specialization and multi-expert activation dilutes it. Therefore, $n=6$ and $k=1$ offer the best trade-off between performance and parameters given the data scale.

Table 5 Ablation study. The *italic font* means the baseline performance of DINOv2-L, and the **bold font** means the best score of CrossEarth-SAR.

Experiments	Components				Performance	
	40K Fully	160K Weakly			mIoU	Gain
Data Construction (DINOv2)	✓				45.1	-14.3
	✓		✓		59.4	+0.0
Training Paradigm		CPT		PEFT	mIoU	Gain
	✓			✓	62.1	+2.7
	✓			✓	62.4	+3.0
Learning Rate	1e-5	3e-5	6e-5	1e-4	mIoU	Gain
	✓				61.2	+1.8
		✓			62.4	+3.0
			✓		62.3	+2.9
			✓	61.9	+2.5	
MoE Design		\mathcal{L}_{BC}		S	mIoU	Gain
	✓				61.1	+1.7
		✓			62.2	+2.8
				✓	61.6	+2.2
	✓		✓	62.4	+3.0	
Expert Number n (Top-k=1)	3	4	5	6	mIoU	Gain
	✓				60.9	+1.5
		✓			61.6	+2.2
			✓		61.9	+2.5
			✓	62.4	+3.0	
Activate Top-k (n=6)	k=1	k=2	k=3		mIoU	Gain
	✓				62.4	+3.0
		✓			61.7	+2.3
			✓	61.3	+0.9	

Table 6 Experiments on the sensitivity of individual physical descriptors to downstream gaps.

Domain Gap	Region	Polarization	Complex Value	Platform	Microwave Band
Test Bench	N2S	VV2F	Cr2R	O2D	S2A
H_{DE}	37.45	73.47	75.75	19.70	59.18
ENL	37.48	73.33	75.97	19.68	59.02
R_{LR}	37.49	73.43	75.91	19.83	59.06

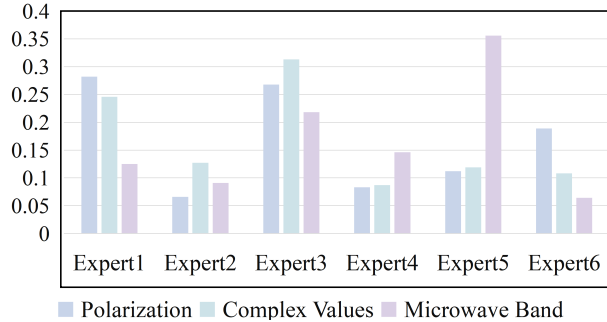


Figure 5 Relationship Between Expert Activations and the SAR Physical Domain.

Physical Descriptors. We enable only one physical descriptor at a time across five domain gaps, evaluating each gap on a representative benchmark. The results on mIoU in Tab. 6 show that H_{DE} is more sensitive to Polarization (73.47%) and Microwave Band (59.18%), ENL to Complex Value (75.97%), and R_{LR} to Region (37.49%) and Platform (19.83%). Additionally, the results show that all 3 physical descriptors are important, and combining them yields better performance, as reported in Tab. 2 and Tab. 3.

Sensitivity of experts to the SAR domain. We randomly selected one benchmark for each of three representative domain gaps to visualise the activation proportions of each expert and the SAR domain layer by layer. As shown in the Fig. 5, polarization is dominated by Expert 1, complex values by Expert 3, and the microwave band by Expert 5.

5.6 Visualization

In this section, we primarily present visualizations of loss and expert activation ratio. Additional visualization results are provided in the Appendix.

Loss Curve in Downstream Tasks. We visualize the loss curves of CrossEarth-SAR-L during downstream fine-tuning. As shown in Fig. 6, CrossEarth-SAR consistently starts and converges at lower losses than DINOv2. In the D2O task, for instance, the initial loss drops from over 64.0 to around 50.0, and the final loss remains lower as training progresses. Similar patterns appear in VV2F, demonstrating the effectiveness of continuous pre-training and its improved scalability in downstream optimization. More visualizations are attached in the Appendix.

Expert Activation Ratio. As shown in Fig. 7, the experts exhibit a clear layer-wise specialization. Experts 3 and 4 dominate the early layers (1–6), indicating their focus on low-level SAR cues such as speckle statistics. In the mid-layers (7–16), Experts 1, 2, 5, and 6 show the highest activation, reflecting their role in modeling geometric structures, textures, and scattering patterns. In the deepest layers (17–24), activation concentrates on Experts 1 and 5, suggesting that they are responsible for high-level semantic learning. These observations show that CrossEarth-SAR learns an effective hierarchical specialization across layers.

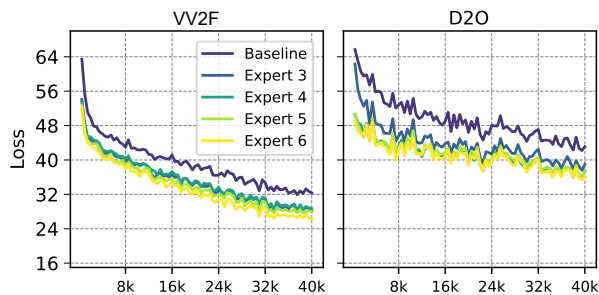


Figure 6 Loss Curve of CrossEarth-SAR in two downstream tasks fine-tuning. CrossEarth-SAR consistently starts and converges at lower losses than DINOv2, illustrating the effectiveness of continuous pre-training across diverse SAR domains.

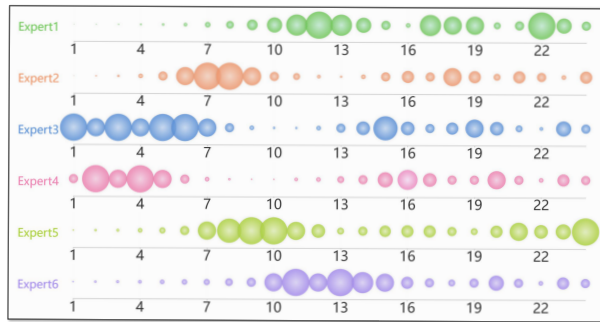


Figure 7 Ratio of expert activations over all benchmarks. For each of the 24 layers, we count how frequently each expert is activated, and larger circles denote higher activation ratios.

6 Conclusion

In this paper, we present **CrossEarth-SAR**, the first **billion-scale** SAR VFM featuring a physics-guided sparse MoE architecture, designed for cross-domain semantic segmentation. Additionally, we construct **CrossEarth-SAR-200K** dataset, which contains over 200K SAR weakly and fully labeled semantic segmentation data, enabling continual pre-training at a global scale for cross-domain semantic understanding. Furthermore, to encourage SAR RSDG research, we also curate a DG benchmark collection with 22 sub-benchmarks, providing rigorous and comprehensive evaluations of models’ generalizability. Experiments validate the superiority and potential of CrossEarth-SAR across regions, polarization, complex values, microwave band, and platform. We hope this work can promote research on cross-domain generalization within the SAR community, and we will continue to explore its DG capabilities in other downstream tasks, such as target recognition and change detection.

References

- [1] Luciano Alparone, Alberto Arienzo, and Fabrizio Lombardini. Improved coherent processing of synthetic aperture radar data through speckle whitening of single-look complex images. *Remote Sensing*, 16(16):2955, 2024.
- [2] Alberto Arienzo, Fabrizio Argenti, Luciano Alparone, and Monica Gherardelli. Accurate despeckling and estimation of polarimetric features by means of a spatial decorrelation of the noise in complex polsar data. *Remote Sensing*, 12(2):331, 2020.
- [3] Bilel Benjdira, Yakoub Bazi, Anis Koubaa, and Ayoub Ammar. Car detection using unmanned aerial vehicles: Image enhancement and domain adaptation. *Remote Sensing*, 11(7):747, 2019. doi: 10.3390/rs11070747.
- [4] Yunlong Chen, Wen Li, Christos Sakaridis, Dengxin Dai, and Luc Van Gool. Domain adaptive semantic segmentation with self-training and uncertainty guidance. In *BMVC*, 2019.
- [5] Yezhen Cong, Samar Khanna, Chenlin Meng, Patrick Liu, Erik Rozi, Yutong He, Marshall Burke, David Lobell, and Stefano Ermon. Satmae: Pre-training transformers for temporal and multi-spectral satellite imagery. *NeurIPS*, 35:197–211, 2022.
- [6] Loïc Denis, Emanuele Dalsasso, and Florence Tupin. A review of deep-learning techniques for sar image restoration. In *2021 IEEE International Geoscience and Remote Sensing Symposium IGARSS*, pages 411–414. IEEE, 2021.
- [7] Alexey Dosovitskiy, Lucas Beyer, Alexander Kolesnikov, Dirk Weissenborn, Xiaohua Zhai, Thomas Unterthiner, Mostafa Dehghani, Matthias Minderer, Georg Heigold, Sylvain Gelly, et al. An image is worth 16x16 words: Transformers for image recognition at scale. *arXiv preprint arXiv:2010.11929*, 2020.
- [8] Ziyang Gong, Fuhao Li, Yupeng Deng, Wenjun Shen, Xianzheng Ma, Zhenming Ji, and Nan Xia. Train one,

- generalize to all: Generalizable semantic segmentation from single-scene to all adverse scenes. In Proceedings of the 31st ACM International Conference on Multimedia, pages 2275–2284, 2023.
- [9] Ziyang Gong, Fuhao Li, Yupeng Deng, Deblina Bhattacharjee, Xianzheng Ma, Xiangwei Zhu, and Zhenming Ji. Coda: Instructive chain-of-domain adaptation with severity-aware visual prompt tuning. In European Conference on Computer Vision, pages 130–148. Springer, 2024.
- [10] Ziyang Gong, Zhixiang Wei, Di Wang, Xianzheng Ma, Hongruixuan Chen, Yuru Jia, Yupeng Deng, Zhenming Ji, Xiangwei Zhu, Naoto Yokoya, et al. Crossearth: Geospatial vision foundation model for domain generalizable remote sensing semantic segmentation. arXiv preprint arXiv:2410.22629, 2024.
- [11] Hao Guan and Mingxia Liu. Domain adaptation for medical image analysis: a survey. IEEE Transactions on Biomedical Engineering, 69(3):1173–1185, 2021.
- [12] Xin Guo, Jiangwei Lao, Bo Dang, Yingying Zhang, Lei Yu, Lixiang Ru, Liheng Zhong, Ziyuan Huang, Kang Wu, Dingxiang Hu, Huimei He, Jian Wang, Jingdong Chen, Ming Yang, Yongjun Zhang, and Yansheng Li. Skysense: A multi-modal remote sensing foundation model towards universal interpretation for earth observation imagery. In Proceedings of the IEEE/CVF Conference on Computer Vision and Pattern Recognition (CVPR), pages 27672–27683, June 2024.
- [13] Lukas Hoyer, Dengxin Dai, and Luc Van Gool. Hrda: Context-aware high-resolution domain-adaptive semantic segmentation. In ECCV, pages 372–391, 2022.
- [14] Xiaoxing Hu, Ziyang Gong, Yupei Wang, Yuru Jia, Gen Luo, and Xue Yang. Earth-adapter: Bridge the geospatial domain gaps with mixture of frequency adaptation. arXiv preprint arXiv:2504.06220, 2025.
- [15] Meiyu Huang, Yao Xu, Lixin Qian, Weili Shi, Yaqin Zhang, Wei Bao, Nan Wang, Xuejiao Liu, and Xueshuang Xiang. The qxs-saropt dataset for deep learning in sar-optical data fusion. arXiv preprint arXiv:2103.08259, 2021.
- [16] John R. Jensen. Introductory Digital Image Processing: A Remote Sensing Perspective. Pearson, Boston, 4 edition, 2015. ISBN 978-0-13-405816-0.
- [17] Yuru Jia, Valerio Marsocci, Ziyang Gong, Xue Yang, Maarten Vergauwen, and Andrea Nascetti. Can generative geospatial diffusion models excel as discriminative geospatial foundation models? arXiv preprint arXiv:2503.07890, 2025.
- [18] Anuj Kumar, Hiesik Kim, and Gerhard P Hancke. Environmental monitoring systems: A review. IEEE Sensors Journal, 13(4):1329–1339, 2012.
- [19] J-S Lee and Igor Jurkevich. Segmentation of sar images. IEEE transactions on Geoscience and Remote Sensing, 27(6):674–680, 2005.
- [20] Fuhao Li, Ziyang Gong, Yupeng Deng, Xianzheng Ma, Renrui Zhang, Zhenming Ji, Xiangwei Zhu, and Hong Zhang. Parsing all adverse scenes: Severity-aware semantic segmentation with mask-enhanced cross-domain consistency. In Proceedings of the AAAI Conference on Artificial Intelligence, volume 38, pages 13483–13491, 2024.
- [21] Weijie Li, Wei Yang, Tianpeng Liu, Yuenan Hou, Yuxuan Li, Zhen Liu, Yongxiang Liu, and Li Liu. Predicting gradient is better: Exploring self-supervised learning for sar atr with a joint-embedding predictive architecture. ISPRS Journal of Photogrammetry and Remote Sensing, 218:326–338, 2024.
- [22] Weijie Li, Wei Yang, Yuenan Hou, Li Liu, Yongxiang Liu, and Xiang Li. Saratr-x: Towards building a foundation model for sar target recognition. IEEE Transactions on Image Processing, 2025.
- [23] Xue Li, Guo Zhang, Hao Cui, Shasha Hou, Shunyao Wang, Xin Li, Yujia Chen, Zhijiang Li, and Li Zhang. Mcanet: A joint semantic segmentation framework of optical and sar images for land use classification. International Journal of Applied Earth Observation and Geoinformation, 106:102638, 2022.
- [24] Yansheng Li, Sijie Liu, Wei Zhou, and et al. Cross-city domain adaptation for semantic segmentation of aerial images. Remote Sensing, 12(19):3132, 2020. doi: 10.3390/rs12193132.
- [25] Yuxuan Li, Xiang Li, Weijie Li, Qibin Hou, Li Liu, Ming-Ming Cheng, and Jian Yang. Sardet-100k: Towards open-source benchmark and toolkit for large-scale sar object detection. Advances in Neural Information Processing Systems, 37:128430–128461, 2024.

- [26] Fan Liu, Delong Chen, Zhangqingyun Guan, Xiacong Zhou, Jiale Zhu, Qiaolin Ye, Liyong Fu, and Jun Zhou. Remoteclip: A vision language foundation model for remote sensing. IEEE Transactions on Geoscience and Remote Sensing, 2024.
- [27] I Loshchilov. Decoupled weight decay regularization. arXiv preprint arXiv:1711.05101, 2017.
- [28] Mostafa Mansourpour, MA Rajabi, and JAR Blais. Effects and performance of speckle noise reduction filters on active radar and sar images. In Proc. Isprs, volume 36, page W41, 2006.
- [29] Dimitrios Marmanis, Mihai Datcu, Thomas Esch, and Uwe Stilla. Classification with an edge: Improving semantic segmentation of aerial images using boundary detection. ISPRS Journal of Photogrammetry and Remote Sensing, 135:158–172, 2018. doi: 10.1016/j.isprsjprs.2017.11.009.
- [30] Ronald McGill. Urban management in developing countries. Cities, 15(6):463–471, 1998.
- [31] Van-Hoai Nguyen, Tom Drummond, Lars Petersson, and Mehrtash Harandi. Domain generalization for land cover mapping with meta-learning. In IGARSS, pages 1156–1159, 2021. doi: 10.1109/IGARSS47720.2021.9554748.
- [32] Maxime Oquab, Timothée Darcet, Théo Moutakanni, Huy Vo, Marc Szafraniec, Vasil Khalidov, Pierre Fernandez, Daniel Haziza, Francisco Massa, Alaaeldin El-Nouby, et al. Dinov2: Learning robust visual features without supervision. arXiv preprint arXiv:2304.07193, 2023.
- [33] Kunpeng Qiu, Zhiqiang Gao, Zhiying Zhou, Mingjie Sun, and Yongxin Guo. Noise-consistent siamese-diffusion for medical image synthesis and segmentation. In Proceedings of the Computer Vision and Pattern Recognition Conference, pages 15672–15681, 2025.
- [34] Kunpeng Qiu, Zhiying Zhou, and Yongxin Guo. Adaptively distilled controlnet: Accelerated training and superior sampling for medical image synthesis. In International Conference on Medical Image Computing and Computer-Assisted Intervention, pages 55–65. Springer, 2025.
- [35] Colorado J Reed, Ritwik Gupta, Shufan Li, Sarah Brockman, Christopher Funk, Brian Clipp, Kurt Keutzer, Salvatore Candido, Matt Uyttendaele, and Trevor Darrell. Scale-mae: A scale-aware masked autoencoder for multiscale geospatial representation learning. In Proceedings of the IEEE/CVF International Conference on Computer Vision, pages 4088–4099, 2023.
- [36] Markus Reichstein, Gustau Camps-Valls, Bjorn Stevens, and et al. Deep learning and process understanding for data-driven earth system science. Nature, 566:195–204, 2019. doi: 10.1038/s41586-019-0912-1.
- [37] Bo Ren, Shibin Ma, Biao Hou, Danfeng Hong, Jocelyn Chanussot, Jianlong Wang, and Licheng Jiao. A dual-stream high resolution network: Deep fusion of gf-2 and gf-3 data for land cover classification. International Journal of Applied Earth Observation and Geoinformation, 112:102896, 2022.
- [38] Laura Dingle Robertson, Heather McNairn, Marco van der Kooij, Xianfeng Jiao, Samuel Ihuoma, and Pamela Joosse. Monitoring autumn agriculture activities using synthetic aperture radar (sar) and coherence change detection. Heliyon, 9(6), 2023.
- [39] Sudipan Saha, Thomas Krauß, and Peter Reinartz. Unsupervised domain adaptation for semantic segmentation of satellite images. In IGARSS, pages 5171–5174, 2020. doi: 10.1109/IGARSS39084.2020.9323954.
- [40] Michael Schmitt, Lloyd H. Hughes, Chenying Qiu, and Xiao Xiang Zhu. Sen12ms – a curated dataset of georeferenced multi-spectral sentinel-1/2 imagery for deep learning and data fusion. In ISPRS Annals, volume IV-2/W7, pages 153–160, 2019. doi: 10.5194/isprs-annals-IV-2-W7-153-2019.
- [41] Xianzheng Shi, Shilei Fu, Jin Chen, Feng Wang, and Feng Xu. Object-level semantic segmentation on the high-resolution gaofen-3 fusar-map dataset. IEEE Journal of Selected Topics in Applied Earth Observations and Remote Sensing, 14:3107–3119, 2021.
- [42] Oriane Siméoni, Huy V Vo, Maximilian Seitzer, Federico Baldassarre, Maxime Oquab, Cijo Jose, Vasil Khalidov, Marc Szafraniec, Seungeun Yi, Michaël Ramamonjisoa, et al. Dinov3. arXiv preprint arXiv:2508.10104, 2025.
- [43] Adam Stewart, Nils Lehmann, Isaac Corley, Yi Wang, Yi-Chia Chang, Nassim Ait Ait Ali Braham, Shradha Sehgal, Caleb Robinson, and Arindam Banerjee. Ssl4eo-l: Datasets and foundation models for landsat imagery. Advances in Neural Information Processing Systems, 36:59787–59807, 2023.

- [44] Di Wang, Jing Zhang, Minqiang Xu, Lin Liu, Dongsheng Wang, Erzhong Gao, Chengxi Han, Haonan Guo, Bo Du, Dacheng Tao, et al. Mtp: Advancing remote sensing foundation model via multi-task pretraining. IEEE Journal of Selected Topics in Applied Earth Observations and Remote Sensing, 2024.
- [45] Di Wang, Meiqi Hu, Yao Jin, Yuchun Miao, Jiaqi Yang, Yichu Xu, Xiaolei Qin, Jiaqi Ma, Lingyu Sun, Chenxing Li, et al. Hypersigma: Hyperspectral intelligence comprehension foundation model. IEEE Transactions on Pattern Analysis and Machine Intelligence, 2025.
- [46] Lei Wang, Xin Xu, Yue Yu, Rui Yang, Rong Gui, Zhaozhao Xu, and Fangling Pu. Sar-to-optical image translation using supervised cycle-consistent adversarial networks. Ieee Access, 7:129136–129149, 2019.
- [47] Mengyu Wang, Hanbo Bi, Yingchao Feng, Linlin Xin, Shuo Gong, Tianqi Wang, Zhiyuan Yan, Peijin Wang, Wenhui Diao, and Xian Sun. A complex-valued sar foundation model based on physically inspired representation learning. arXiv preprint arXiv:2504.11999, 2025.
- [48] Y. Wang, H. Liu, and J. Zhang. Semantic segmentation of sar images with transformer-based networks. Remote Sensing, 14(3):512, 2022. doi: 10.3390/rs14030512.
- [49] Yuanyuan Wang and Xiao Xiang Zhu. The sarptical dataset for joint analysis of sar and optical image in dense urban area. In IGARSS 2018-2018 IEEE International Geoscience and Remote Sensing Symposium, pages 6840–6843. IEEE, 2018.
- [50] Zhirui Wang, Xuan Zeng, Zhiyuan Yan, Jian Kang, and Xian Sun. Air-polsar-seg: A large-scale data set for terrain segmentation in complex-scene polsar images. IEEE Journal of Selected Topics in Applied Earth Observations and Remote Sensing, 15:3830–3841, 2022.
- [51] U Wegmüller, M Santoro, F Mattia, A Balenzano, G Satalino, P Marzahn, G Fischer, R Ludwig, and N Floury. Progress in the understanding of narrow directional microwave scattering of agricultural fields. Remote Sensing of Environment, 115(10):2423–2433, 2011.
- [52] Kan Wei, Jinkun Dai, Danfeng Hong, and Yuanxin Ye. Mgfnet: An mlp-dominated gated fusion network for semantic segmentation of high-resolution multi-modal remote sensing images. International Journal of Applied Earth Observation and Geoinformation, 135:104241, 2024.
- [53] Zhixiang Wei, Lin Chen, Yi Jin, Xiaoxiao Ma, Tianle Liu, Pengyang Ling, Ben Wang, Huaian Chen, and Jinjin Zheng. Stronger fewer & superior: Harnessing vision foundation models for domain generalized semantic segmentation. In CVPR, pages 28619–28630, June 2024.
- [54] Fan Wu, Chao Wang, Hong Zhang, Juanjuan Li, Lu Li, Weirong Chen, and Bo Zhang. Built-up area mapping in china from gf-3 sar imagery based on the framework of deep learning. Remote Sensing of Environment, 262: 112515, 2021.
- [55] Kang Wu, Yingying Zhang, Lixiang Ru, Bo Dang, Jiangwei Lao, Lei Yu, Junwei Luo, Zifan Zhu, Yue Sun, Jiahao Zhang, Qi Zhu, Jian Wang, Ming Yang, Jingdong Chen, Yongjun Zhang, and Yansheng Li. A semantic-enhanced multi-modal remote sensing foundation model for earth observation. Nature Machine Intelligence, 7:1235–1249, 2025. doi: 10.1038/s42256-025-01078-8.
- [56] Lin Wu, Hongxia Wang, Yuan Li, Zhengwei Guo, and Ning Li. A novel method for layover detection in mountainous areas with sar images. Remote Sensing, 13(23):4882, 2021.
- [57] Junshi Xia, Naoto Yokoya, Bruno Adriano, and Clifford Broni-Bediako. Openearthmap: A benchmark dataset for global high-resolution land cover mapping. In Proceedings of the IEEE/CVF Winter Conference on Applications of Computer Vision, pages 6254–6264, 2023.
- [58] Yuming Xiang, Rongshu Tao, Feng Wang, Hongjian You, and Bing Han. Automatic registration of optical and sar images via improved phase congruency model. IEEE Journal of Selected Topics in Applied Earth Observations and Remote Sensing, 13:5847–5861, 2020.
- [59] Enze Xie, Wenhai Wang, Zhiding Yu, Anima Anandkumar, Jose M Alvarez, and Ping Luo. Segformer: Simple and efficient design for semantic segmentation with transformers. NeurIPS, 34:12077–12090, 2021.
- [60] Zhitong Xiong, Yi Wang, Fahong Zhang, Adam J Stewart, Joëlle Hanna, Damian Borth, Ioannis Papoutsis, Bertrand Le Saux, Gustau Camps-Valls, and Xiao Xiang Zhu. Neural plasticity-inspired foundation model for observing the earth crossing modalities. CoRR, 2024.

- [61] JIN Yan, QIU Xiaolan, PAN Jie, SHANGGUAN Songtao, WANG Zezhong, WANG Wei, and YANG Hong. Mpolsar-1.0: Multidimensional sar multiband fully polarized fine classification dataset. Journal of Radars, 13(3): 525–538, 2024.
- [62] Yi Yang, Xiaokun Zhang, Qingchen Fang, Jing Liu, Ziqi Ye, Rui Li, Li Liu, and Haipeng Wang. Fusar-klip: Towards multimodal foundation models for remote sensing, 2025. URL <https://arxiv.org/abs/2509.23927>.
- [63] Ziqi Ye, Xiayang Xiao, and Haipeng Wang. Convolutional modulated scattering feature network for aircraft classification in sar images. In IGARSS 2024-2024 IEEE International Geoscience and Remote Sensing Symposium, pages 9329–9332. IEEE, 2024.
- [64] Pan Zhang, Baochai Peng, Chaoran Lu, Quanjin Huang, and Dongsheng Liu. Asanet: Asymmetric semantic aligning network for rgb and sar image land cover classification. ISPRS Journal of Photogrammetry and Remote Sensing, 218:574–587, 2024.
- [65] Runpei Zhang, Zhen Li, Qiang Wang, and et al. Personalize segment anything model for remote sensing zero/few-shot segmentation. arXiv preprint arXiv:2306.05457, 2023.
- [66] X. Zhang, Y. Wang, C. Li, and et al. Hypersigma: A foundation model for hyperspectral and multispectral remote sensing. arXiv preprint arXiv:2405.12667, 2024.
- [67] Xiaosong Zhang, Yunjie Tian, Lingxi Xie, Wei Huang, Qi Dai, Qixiang Ye, and Qi Tian. Hivit: A simpler and more efficient design of hierarchical vision transformer. In The eleventh international conference on learning representations, 2023.
- [68] Yingying Zhang, Lixiang Ru, Kang Wu, Lei Yu, Lei Liang, Yansheng Li, and Jingdong Chen. Skysense v2: A unified foundation model for multi-modal remote sensing. arXiv preprint arXiv:2507.13812, 2025.
- [69] NR Zheng, Z Yang, Z Shi, H Yang, Y Sun, and F Wang. Airborne multi-dimensional sar land cover dataset and fusion classification method. National Remote Sensing Bulletin, 2023.
- [70] WANG Zhirui, ZHAO Liangjin, WANG Yuelei, ZENG Xuan, KANG Jian, YANG Jian, and SUN Xian. Airpolsar-seg-2.0: Polarimetric sar ground terrain classification dataset for large-scale complex scenes. Journal of Radars, 14(2):353–365, 2025.
- [71] Jun-Yan Zhu, Taesung Park, Phillip Isola, and Alexei A. Efros. Unpaired image-to-image translation using cycle-consistent adversarial networks. In ICCV, pages 2242–2251, 2017. doi: 10.1109/ICCV.2017.244.
- [72] Yang Zou, Zhiding Yu, B.V.K. Vijaya Kumar, and Jinsong Wang. Unsupervised domain adaptation for semantic segmentation via class-balanced self-training. In ECCV, pages 289–305, 2018. doi: 10.1007/978-3-030-01219-9_18.
- [73] Yang Zou, Zhiding Yu, Xinkun Liu, B.V.K. Vijaya Kumar, and Jinsong Wang. Confidence regularized self-training. In ICCV, pages 5982–5991, 2019. doi: 10.1109/ICCV.2019.00608.

Appendix

A CrossEarth-SAR-200K

CrossEarthSAR-200K is composed of three parts: The 37K private SAR-optical paired dataset named CrossEarth-OPT-SAR, 126K publicly available SAR-optical paired datasets, and 40K publicly available SAR segmentation datasets. Among these data, 126,169 unlabeled images are drawn from QXS-SAROPT [15], WHU-SEN-City [46], SEN12 [40], Osdataset [58], and SARptical [49]. Moreover, 40,042 labeled images are drawn from AIR-PolSAR-Seg 1.0 [50], AIR-MDSAR-Map [69], DDHR-X [37], and MPOLSAR 1.0 [61]. These data are released by or collected from different countries and institutions. Therefore, the data sources are extremely diverse, covering virtually all major regions around the world.

For data without semantic segmentation labels, the strongest RSDG model CrossEarth, is adopted to segment the optical images paired with SAR images. The R2U weights trained on 7 classes from the Loveda dataset are used. The resulting predictions are assigned as labels for the corresponding SAR images. Furthermore, all SAR images are cropped or resized to a resolution of five hundred twelve pixels. CrossEarth-SAR-200K-Val is randomly selected as validation for continuous pre-training.

The CrossEarthSAR-200K dataset comprises a total of 203,240 images with corresponding pixel-level annotations, covering seven semantic classes: building, road, water, barren, forest, agricultural, and background. To the best of our knowledge, CrossEarthSAR-200K is the first large-scale SAR semantic segmentation dataset, and its size surpasses that of the widely used COCO-Stuff benchmark (164K images) for general-purpose semantic segmentation. The scale and diversity of CrossEarthSAR-200K effectively emulate real-world deployment scenarios in which SAR semantic segmentation models are applied across multiple data sources, with imagery collected from 109 regions worldwide. CrossEarthSAR-200K provides a robust foundation for training and evaluation, thereby advancing research in SAR semantic segmentation and image understanding. The composition and introduction of the CrossEarthSAR-200K are shown in Tab. 7.

To quantitatively evaluate the confidence of generated pseudo-labels in remote sensing semantic segmentation, we propose a metric called “Mean Agreement” that measures the consistency of predictions across multiple foundation models. This metric is calculated as follows:

Let $\mathcal{I} = \{I_1, I_2, \dots, I_N\}$ represent a set of N optical images sampled from the unlabeled portion of the CrossEarth-SAR-200K dataset, where we set $N = 1000$ in our experiments. For each image I_i , we denote its total number of pixels as $|I_i|$. Let $\mathcal{M} = \{M_1, M_2, M_3, M_4\}$ represent the set of four foundation models used for semantic segmentation (SatMAE, ScaleMAE, MTP, and CrossEarth).

For each pixel position (x, y) in image I_i , let $M_j(I_i, x, y) \in \{1, 2, \dots, 7\}$ denote the class label predicted by model M_j , where 7 represents the number of semantic categories in our task. We define the agreement indicator function \mathcal{A} for pixel (x, y) as:

$$\mathcal{A}(I_i, x, y) = \begin{cases} 1, & \text{if } M_1(I_i, x, y) = M_2(I_i, x, y) = M_3(I_i, x, y) = M_4(I_i, x, y) \\ 0, & \text{otherwise} \end{cases}$$

The agreement ratio R_i for image I_i is calculated as:

$$R_i = \frac{\sum_{x,y} \mathcal{A}(I_i, x, y)}{|I_i|}$$

Finally, the Mean Agreement across all N images is defined as:

$$\text{Mean Agreement} = \frac{1}{N} \sum_{i=1}^N R_i$$

Table 7 CrossEarth-SAR-200K source datasets information. Res.:Resolution. GF-3: Gaofen-3. S-1: Sentinel-1. T-X: TerraSAR-X. Air: Airborne SAR.

Datasets	Resolution (m)	Band	Polarization	Satellites
QXS-SAROPT [15]	1m	C	VV	Gaofen-3
WHU-SEN-City [46]	20-22m	C	VV, VH	Sentinel-1
SEN12 [40]	10m	C	VV, VH	Sentinel-1
Osdataset [58]	1m	C	VV	Gaofen-3
SARptical [49]	1m	X	VV, HH	TerraSAR-X
DDHR-X [37]	1m	C	VV	Gaofen-3
MPOLSAR-1.0 [61]	0.5-1m	P, L, S, C, X	HH, HV, VH, VV	Airborne SAR
AIR-MDSAR-Map [69]	0.2-1m	P, L, S, C	HH, HV, VH, VV	Airborne SAR
AIR-PoSAR-Seg 1.0 [50]	8m	C	HH, HV, VH, VV	Gaofen-3
CrossEarth-OPT-SAR	0.5-3m	X	HH	HT-1

This metric quantifies the proportion of pixels where all four foundation models (SatMAE, ScaleMAE, MTP, and CrossEarth) agree on the same semantic class. A higher Mean Agreement value indicates greater consistency among the models’ predictions, suggesting higher confidence in the generated pseudo-labels. This approach leverages the collective intelligence of multiple strong foundation models to assess the reliability of semantic segmentation results in the absence of ground truth labels.

B Results

For the one gap benchmarks, the detailed per-category performance of different methods on the N2S, S2N, K2C and C2K benchmarks are reported in Tab. 8. The detailed per-category performance of different methods on the VV2F, F2VV, HH2F and F2HH benchmarks are reported in Tab. 9. Additionally, the detailed per-category performance of different methods on the C(r)2R, R2C(r), C(i)2R and R2C(i) benchmarks are reported in Tab. 10.

For the two gaps benchmarks, the detailed per-category performance of different methods on the F2A, A2F, O2D and D2O benchmarks are reported in Tab. 11.

For the three gaps benchmarks, the detailed per-category performance of different methods on the D2F, F2D, W2D and D2W benchmarks are reported in Tab. 12.

These results further demonstrate that CrossEarth-SAR achieves state-of-the-art robustness across regions, radar bands, and polarization modes, as well as superior performance on multi-gaps SAR RSDG tasks.

C Visualization

Fig. 9 and Fig. 10 respectively present the performance of CrossEarth-SAR under one-gap and multi-gap settings, demonstrating its strong superiority over competing methods. Overall, these visual prediction maps provide an intuitive representation of the qualitative findings. Based on this comprehensive set of experiments, we conclude that while CrossEarth is more effective in all gaps than current other models, there are still many challenges to be addressed in SAR RSDG research.

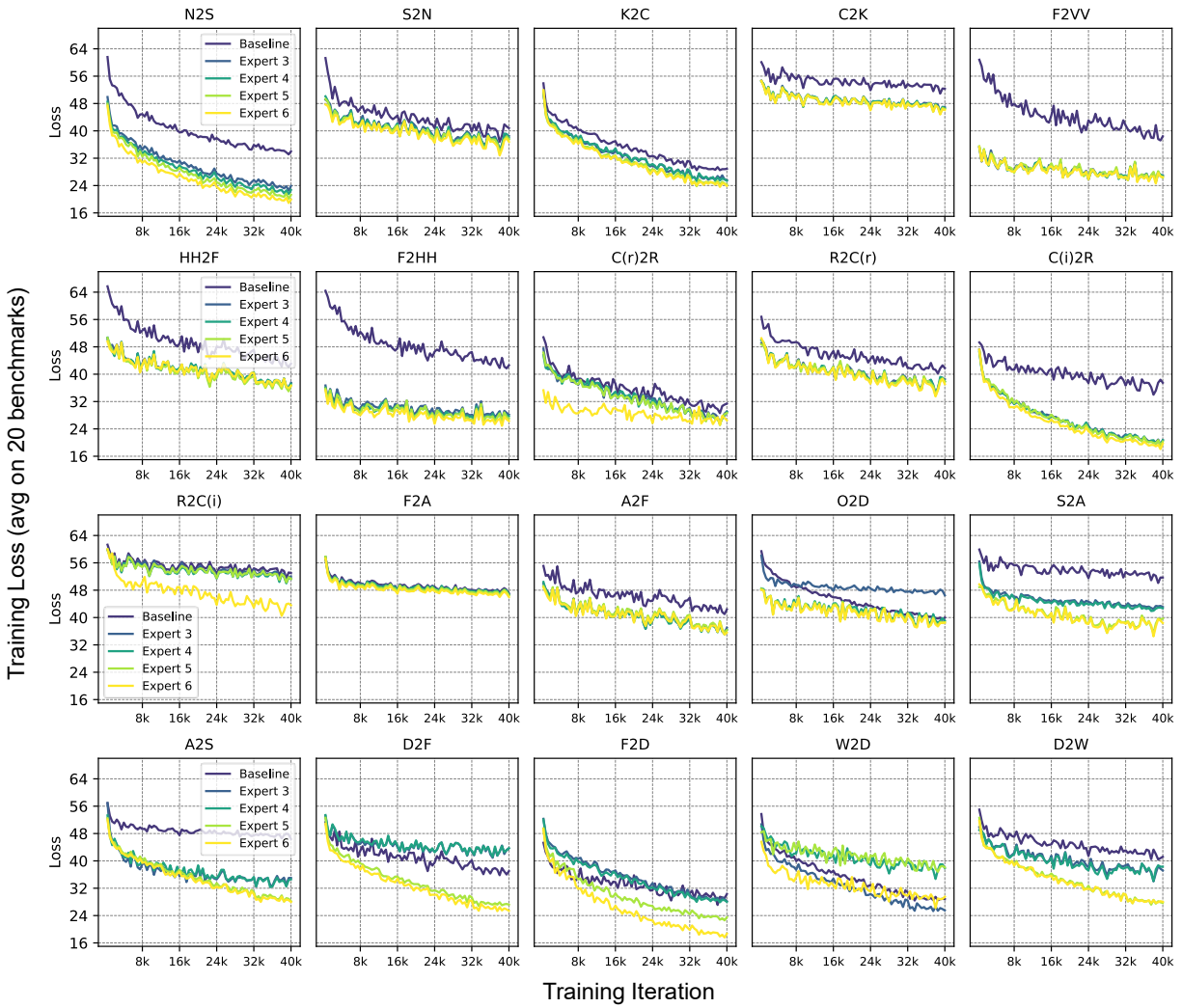


Figure 8 Loss Curve of CrossEarth-SAR in other 20 downstream tasks fine-tuning. CrossEarth-SAR consistently starts and converges at lower losses than Baseline, illustrating the effectiveness of CPT across diverse SAR domains.

Table 8 Performance comparison on benchmark for gaps1-1. **Bolds** = best; underlines = second best. Bldg:Bulidings. Grnd:Ground. Road:Roads. Veg:Vegetation. Wtr:Water. Farm:Farmland. Green:Greenery. Otr:Others.

Method	Backbone	Domain		Classes				mIoU (%)	Domain		Classes				mIoU (%)			
		Source	→ Unseen	Bldg	Grnd	Road	Veg		Wtr	Source	→ Unseen	Bldg	Farm	Green		Otr	Road	Wtr
SARATR-X [13]	HViT-B [59]			55.6	5.7	23.1	31.6	20.3	28.4			35.5	0.0	0.0	0.0	0.0	0.0	5.9
S12-MoCo [43]	ViT-S [7]			54.1	3.9	7.3	32.3	31.6	23.2			37.4	0.0	16.1	0.0	0.0	0.0	8.9
S12-DINO [43]	ViT-S [7]			48.0	4.0	3.6	32.6	35.8	22.5			43.1	0.0	12.9	0.0	0.2	19.6	12.6
S12-MAE [43]	ViT-S [7]			48.5	4.1	5.2	28.7	28.6	22.9			35.5	0.0	0.0	0.0	0.0	0.0	5.9
DOFA [60]	ViT-B [7]			53.0	12.9	10.3	28.9	21.4	25.3			54.1	0.0	23.3	0.0	0.0	17.3	15.8
SatMAE [5]	ViT-L [7]			55.2	5.6	7.7	32.5	36.0	26.2			60.2	0.0	23.9	0.0	0.0	12.0	14.5
ScaleMAE [35]	ViT-L [7]			55.7	6.2	15.5	30.9	32.4	26.4			51.1	0.0	17.6	0.0	0.1	8.5	12.9
RemoteCLIP [26]	ViT-L [7]			45.4	3.5	3.4	29.8	30.0	22.4			35.5	0.0	0.0	0.0	0.0	0.0	5.9
MTP [44]	ViT-L [7]			59.0	11.9	30.7	34.0	17.1	30.6			68.1	16.3	28.4	0.4	11.2	29.8	25.7
DINOv2 [53]	ViT-L [7]			<u>60.6</u>	17.8	26.5	35.1	21.4	32.3			68.2	50.1	4.8	1.8	30.5	48.3	34.0
DINOv3 [42]	ViT-L [7]			61.47	7.6	22.4	33.3	15.7	33.7			64.2	15.9	<u>27.2</u>	0.7	0.0	41.1	29.9
CrossEarth-SAR-S	ViT-S [7]			56.5	<u>17.0</u>	35.8	35.2	28.3	34.6 (+2.3)			67.9	45.6	11.2	<u>2.8</u>	29.0	56.1	35.4 (+1.4)
CrossEarth-SAR-B	ViT-B [7]			56.4	12.3	35.5	39.1	<u>45.1</u>	36.7 (+4.4)			<u>69.6</u>	45.0	15.5	2.6	36.3	<u>56.6</u>	37.7 (+3.7)
CrossEarth-SAR-L	ViT-L [7]			56.1	13.2	<u>39.0</u>	<u>37.7</u>	49.8	37.8 (+5.5)			68.5	41.4	20.4	1.6	35.9	54.6	38.1 (+4.1)
CrossEarth-SAR-L*	ViT-L [7]			56.4	14.7	40.9	36.6	41.2	38.0 (+5.7)			71.5	<u>49.4</u>	13.2	3.2	36.4	61.1	39.1 (+5.1)
SARATR-X [13]	HViT-B [59]			53.0	11.4	30.3	60.2	19.1	34.8			42.5	0.0	9.5	0.0	0.1	20.6	12.1
S12-MoCo [43]	ViT-S [7]			38.6	0.0	0.3	59.5	24.5	24.0			54.8	0.0	33.2	0.0	0.0	23.5	18.6
S12-DINO [43]	ViT-S [7]			45.2	4.9	8.8	52.2	23.7	27.0			62.3	10.5	36.0	0.0	0.3	75.5	30.8
S12-MAE [43]	ViT-S [7]			49.9	6.2	13.5	55.6	24.3	29.9			72.7	<u>29.6</u>	17.8	0.0	4.5	84.4	34.8
DOFA [60]	ViT-B [7]			47.4	6.7	15.1	43.5	24.9	27.5			71.7	15.3	27.5	0.0	3.4	73.3	31.9
SatMAE [5]	ViT-L [7]			53.4	15.5	15.7	54.6	21.1	32.1			68.0	0.0	43.7	0.0	6.8	81.8	33.4
ScaleMAE [35]	ViT-L [7]			56.5	1.7	9.0	55.6	13.1	27.2			58.4	0.0	<u>39.8</u>	0.0	4.9	79.5	30.5
RemoteCLIP [26]	ViT-L [7]			46.8	6.5	15.7	54.6	27.1	30.2			68.3	15.8	29.6	0.0	0.0	65.3	29.8
MTP [44]	ViT-L [7]			50.8	13.9	33.5	60.5	17.6	35.3			70.2	21.1	23.6	0.0	8.5	80.0	33.9
DINOv2 [53]	ViT-L [7]			55.0	<u>28.3</u>	34.4	63.2	38.2	43.8			74.1	28.2	15.2	0.0	10.2	<u>87.7</u>	35.8
DINOv3 [42]	ViT-L [7]			51.4	15.8	27.7	60.4	33.7	42.8			71.3	21.7	21.7	0.0	7.8	87.4	35.3
CrossEarth-SAR-S	ViT-S [7]			51.8	19.7	41.2	65.3	39.1	43.2 (-0.6)			75.6	30.7	15.9	0.1	13.9	86.6	35.6 (-0.2)
CrossEarth-SAR-B	ViT-B [7]			53.9	13.7	43.6	61.8	<u>45.3</u>	43.4 (-0.4)			77.4	29.1	15.4	0.1	<u>18.5</u>	85.6	37.1 (+1.3)
CrossEarth-SAR-L	ViT-L [7]			52.8	9.0	42.4	63.4	45.7	45.6 (+1.8)			<u>75.7</u>	26.8	15.1	<u>0.1</u>	19.0	83.9	38.4 (+2.6)
CrossEarth-SAR-L*	ViT-L [7]			<u>55.8</u>	29.3	<u>43.1</u>	<u>63.7</u>	41.6	46.7 (+2.9)			74.6	28.9	20.3	0.1	18.3	89.4	38.6 (+2.8)

Table 9 Performance comparison on benchmark for gaps1-2. **Bolds** = best; underlines = second best. Bldg:Bulidings. Grnd:Ground. Mnt:Mountain. Veg:Vegetation. Wtr:Water.

Method	Backbone	Domain		Classes				mIoU (%)	Domain		Classes				mIoU (%)				
		Source	→ Unseen	Bldg	Grnd	Mnt	Road		Veg	Wtr	Source	→ Unseen	Bldg	Grnd		Mnt	Road	Veg	Wtr
SARATR-X [13]	HViT-B [59]			67.3	35.0	81.7	49.3	58.3	51.2	57.1			61.0	23.4	73.3	33.4	55.7	44.6	48.6
S12-MoCo [43]	ViT-S [7]			10.5	14.6	27.2	3.5	40.2	35.6	21.9			4.3	11.9	33.6	2.6	38.2	28.5	19.8
S12-DINO [43]	ViT-S [7]			21.3	7.4	41.8	2.3	32.1	32.8	23.0			33.0	0.6	0.4	1.6	32.8	25.8	15.7
S12-MAE [43]	ViT-S [7]			2.8	3.8	4.0	1.1	36.2	28.6	12.8			3.4	4.8	7.0	0.9	35.4	24.1	12.6
DOFA [60]	ViT-B [7]			46.2	0.8	0.3	0.3	45.5	29.4	20.4			52.0	2.4	0.0	0.3	48.6	26.5	21.6
SatMAE [5]	ViT-L [7]			16.0	5.4	36.2	10.0	31.3	35.9	22.5			10.4	5.7	17.4	9.2	33.1	26.9	17.1
ScaleMAE [35]	ViT-L [7]			11.0	3.8	11.5	13.8	35.4	15.2	15.1			16.6	4.5	15.0	17.1	22.5	13.8	14.9
RemoteCLIP [26]	ViT-L [7]			20.1	1.5	0.0	0.3	24.5	33.5	13.3			24.3	5.0	1.4	0.2	20.4	26.5	13.0
MTP [44]	ViT-L [7]			40.1	6.4	21.9	32.1	32.4	49.5	30.4			15.3	7.8	72.8	22.9	38.7	58.6	36.0
DINOv2 [53]	ViT-L [7]			69.4	37.1	87.1	48.5	67.2	84.9	65.7			70.7	34.5	76.2	44.4	66.9	81.7	56.8
DINOv3 [42]	ViT-L [7]			20.7	19.4	64.9	17.9	42.9	47.0	48.3			5.1	20.9	64.4	17.2	39.8	34.7	50.6
CrossEarth-SAR-S	ViT-S [7]			72.1	50.7	<u>91.0</u>	55.7	71.3	<u>87.0</u>	71.3 (+5.6)			62.5	53.1	90.1	53.0	65.4	86.6	68.5 (+11.7)
CrossEarth-SAR-B	ViT-B [7]			77.4	58.8	89.6	57.9	<u>75.8</u>	84.0	73.5 (+7.8)			<u>73.4</u>	52.8	84.9	52.5	73.0	87.1	70.6 (+13.8)
CrossEarth-SAR-L	ViT-L [7]			76.3	52.7	90.6	55.8	73.5	86.6	73.8 (+8.1)			73.7	55.9	<u>90.1</u>	<u>53.3</u>	<u>72.8</u>	<u>86.9</u>	72.3 (+15.5)
CrossEarth-SAR-L*	ViT-L [7]			<u>77.3</u>	<u>57.5</u>	91.5	<u>56.5</u>	76.0	88.0	73.9 (+8.2)			73.0	<u>55.6</u>	91.2	55.2	71.3	84.4	<u>71.8 (+15.0)</u>
SARATR-X [13]	HViT-B [59]			59.5	36.8	78.8	40.0	59.1	64.7	56.5			64.3	32.3	76.1	35.0	61.5	68.2	56.2
S12-MoCo [43]	ViT-S [7]			19.4	1.5	0.2	2.2	40.5	33.0	16.1			54.7	3.9	27.4	3.4	46.0	52.2	29.9
S12-DINO [43]	ViT-S [7]			57.8	18.0	26.7	12.8	41.8	68.1	37.5			60.2	9.3	40.1	12.5	31.8	56.5	35.1
S12-MAE [43]	ViT-S [7]			34.8	0.0	3.9	1.0	39.8	26.8	17.7			31.4	1.6	1.4	1.4	28.9	28.9	15.6
DOFA [60]	ViT-B [7]			34.0	13.9	24.0	13.8	44.9	53.3	30.7			49.2	11.4	31.7	19.1	33.3	39.0	30.6
SatMAE [5]	ViT-L [7]			52.4	11.5	22.1	12.6	37.5	64.4	33.4			62.6	7.7	24.0	10.1	42.9	32.8	30.0
ScaleMAE [35]	ViT-L [7]			17.5	10.1	67.9	6.7	41.8	55.8	33.3			20.5	6.2	2.6	7.8	38.5	45.6	20.2
RemoteCLIP [26]	ViT-L [7]			33.1	7.5	4.7	3.6	37.0	39.5	20.9			36.3	4.1	6.5	2.3	29.1	25.2	17.3
MTP [44]	ViT-L [7]			50.2	20.5	37.4	19.7	53.7	64.7	40.2			57.6	17.0	27.9	22.9	23.7	24.3	28.9
DINOv2 [53]	ViT-L [7]			67.9	34.0	87.4	44.8	63.5	81.8	63.2			68.9	15.6	76.2	35.6	63.4	71.4	55.2
DINOv3 [42]	ViT-L [7]			66.9	32.1	72.5	37.6	61.6	68.9	56.6			64.4	25.5	59.0	30.7	50.0	67.2	60.4
CrossEarth-SAR-S	ViT-S [7]			73.1	41.5	86.5	49.9	70.4	86.7	68.0 (+4.8)			65.0	30.9	90.4	44.2	66.4	<u>85.3</u>	65.0 (+9.8)
CrossEarth-SAR-B	ViT-B [7]			<u>74.8</u>	<u>48.4</u>	91.2	<u>51.9</u>	<u>73.5</u>	86.4	68.2 (+5.0)			66.4	<u>34.2</u>	86.2	<u>49.5</u>	<u>69.5</u>	<u>84.7</u>	66.5 (+11.3)
CrossEarth-SAR-L	ViT-L [7]			74.1	42.7	<u>92.6</u>	50.1	72.5	86.8	69.8 (+6.6)			72.6	30.2	<u>88.2</u>	47.7	65.0	84.1	67.1 (+11.9)
CrossEarth-SAR-L*	ViT-L [7]			75.6	52.6	93.1	55.2	73.9	87.7	72.2 (+9.0)			<u>69.4</u>	46.8	86.1	52.6	71.0	85.9	68.6 (+13.4)

Table 10 Performance comparison on benchmark for gaps1-3. **Bolds** = best; underlines = second best. Bldg:Buildings. Grnd:Ground. Mnt:Mountain. Veg:Vegetation. Wtr:Water.

Method	Backbone	Domain		Classes				mIoU (%)	Domain		Classes				mIoU (%)				
		Source → Unseen	Unseen	Bldg	Grnd	Mnt	Road		Veg	Wtr	Source → Unseen	Unseen	Bldg	Grnd		Mnt	Road	Veg	Wtr
SARATR-X [13]	HiViT-B [59]			71.0	24.2	0.0	34.7	61.3	60.4	73.8			74.0	31.6	22.0	37.8	66.0	63.5	72.3
S12-MoCo [43]	ViT-S [7]			59.3	12.4	0.9	7.6	47.0	52.4	29.9			59.1	8.0	1.0	7.7	49.2	51.0	29.3
S12-DINO [43]	ViT-S [7]			56.2	4.7	0.0	1.6	46.1	41.5	25.0			54.9	4.3	0.0	2.0	41.3	37.8	23.4
S12-MAE [43]	ViT-S [7]			53.8	3.7	0.0	0.8	46.3	37.4	23.7			49.7	0.9	0.0	0.3	31.0	35.4	19.5
DOFA [60]	ViT-B [7]			54.3	4.8	0.1	0.6	47.1	40.8	24.6			54.3	8.9	0.0	0.3	45.1	39.5	24.7
SatMAE [5]	ViT-L [7]			62.2	22.2	59.5	17.9	50.4	66.0	46.4			61.7	24.5	34.3	22.0	49.0	68.9	43.4
ScaleMAE [35]	ViT-L [7]			62.7	16.5	7.8	15.6	50.6	67.4	36.8			63.6	21.5	66.0	26.5	51.9	70.7	50.0
RemoteCLIP [26]	ViT-L [7]			53.6	4.5	0.0	2.7	38.1	34.9	22.3			50.2	3.1	0.0	0.9	36.6	32.6	20.6
MTP [44]	ViT-L [7]			<u>76.7</u>	<u>54.5</u>	<u>82.3</u>	<u>55.8</u>	<u>70.5</u>	<u>85.0</u>	<u>70.8</u>			<u>77.9</u>	<u>55.4</u>	<u>80.2</u>	<u>56.3</u>	<u>72.8</u>	<u>85.6</u>	<u>71.4</u>
DINOv2 [53]	ViT-L [7]			76.2	51.4	88.3	54.4	71.7	85.5	71.3			77.1	53.0	<u>87.3</u>	54.6	72.2	<u>86.3</u>	71.7
DINOv3 [42]	ViT-L [7]			75.9	50.1	85.2	51.0	70.5	83.7	69.9			76.1	50.5	87.2	50.0	70.9	80.8	69.2
CrossEarth-SAR-S	ViT-S [7]			79.4	54.9	91.8	57.7	<u>76.8</u>	86.6	74.5 (+3.2)			74.1	80.2	50.6	<u>92.6</u>	57.9	77.4	74.2 (+2.5)
CrossEarth-SAR-B	ViT-B [7]			<u>79.4</u>	<u>63.1</u>	<u>91.9</u>	<u>58.4</u>	76.4	87.4	76.1 (+4.8)			76.4	<u>80.0</u>	62.7	92.5	58.3	77.2	75.1 (+3.4)
CrossEarth-SAR-L	ViT-L [7]			79.1	55.5	<u>92.5</u>	57.8	75.6	86.3	76.4 (+5.1)			79.1	57.1	91.7	58.2	75.3	86.3	<u>76.4</u> (+4.7)
CrossEarth-SAR-L*	ViT-L [7]			79.8	65.6	93.5	60.6	76.9	<u>87.2</u>	<u>76.9</u> (+5.6)			76.7	79.9	61.1	93.7	60.7	77.4	76.7 (+5.0)
SARATR-X [13]	HiViT-B [59]			62.1	20.2	29.3	24.5	62.2	47.7	73.4			77.6	58.8	84.2	<u>56.5</u>	76.7	86.7	72.4
S12-MoCo [43]	ViT-S [7]			58.2	27.8	55.5	21.1	59.6	66.1	48.1			55.6	24.0	26.7	8.8	56.6	54.3	37.7
S12-DINO [43]	ViT-S [7]			66.8	34.9	79.4	28.1	66.3	78.3	59.0			64.7	30.5	76.5	20.6	64.2	73.3	55.0
S12-MAE [43]	ViT-S [7]			53.4	12.2	18.7	2.7	55.2	57.8	33.3			46.3	4.8	0.0	1.3	48.2	36.5	22.8
DOFA [60]	ViT-B [7]			49.4	25.2	57.3	8.6	54.3	61.0	42.6			46.6	19.0	8.7	1.3	48.7	33.6	26.3
SatMAE [5]	ViT-L [7]			62.9	14.8	2.6	1.7	58.4	66.0	34.4			44.6	21.9	29.9	7.3	50.2	59.7	35.6
ScaleMAE [35]	ViT-L [7]			36.7	25.3	48.4	27.9	47.2	58.1	40.6			35.4	24.7	19.0	20.3	41.4	42.6	30.6
RemoteCLIP [26]	ViT-L [7]			52.2	7.5	0.3	3.5	50.1	36.0	24.9			58.5	14.4	13.8	6.8	55.9	36.7	31.0
MTP [44]	ViT-L [7]			68.5	51.8	77.4	<u>45.7</u>	68.2	80.6	65.4			71.2	50.7	82.2	47.8	70.6	83.4	67.6
DINOv2 [53]	ViT-L [7]			70.5	55.7	84.0	45.5	71.0	<u>86.2</u>	68.8			70.7	54.4	72.8	46.7	70.2	86.2	66.8
DINOv3 [42]	ViT-L [7]			68.1	52.8	79.6	47.8	68.9	83.9	71.9			67.8	56.0	76.0	46.8	69.7	84.5	66.8
CrossEarth-SAR-S	ViT-S [7]			75.2	59.4	<u>90.4</u>	<u>54.6</u>	75.1	87.2	73.6 (+4.8)			75.3	56.6	<u>89.5</u>	54.0	74.9	87.5	72.9 (+6.1)
CrossEarth-SAR-B	ViT-B [7]			<u>75.9</u>	<u>64.0</u>	90.0	53.8	<u>75.6</u>	87.9	74.5 (+5.7)			76.0	<u>60.9</u>	88.0	53.3	<u>75.5</u>	<u>88.0</u>	73.5 (+6.7)
CrossEarth-SAR-L	ViT-L [7]			74.2	55.3	<u>81.7</u>	51.7	<u>73.3</u>	<u>87.2</u>	76.4 (+7.6)			<u>74.4</u>	57.2	<u>89.2</u>	<u>52.0</u>	<u>74.0</u>	87.5	73.6 (+6.8)
CrossEarth-SAR-L*	ViT-L [7]			77.4	65.6	91.9	56.7	77.2	8.3	76.7 (+7.9)			<u>77.4</u>	65.1	90.2	56.9	77.2	88.5	75.1 (+8.3)

Table 11 Performance comparison on benchmark for gaps2. **Bolds** = best; underlines = second best. Bldg:Buildings. Otr:Others. Veg:Vegetation. Wtr:Water. Green:Greenery.

Method	Backbone	Domain		Classes				mIoU (%)	Domain		Classes				mIoU (%)			
		Source → Unseen	Unseen	Bldg	Otr	Road	Veg		Wtr	Source → Unseen	Unseen	Bldg	Farm	Green		Otr	Road	Wtr
SARATR-X [13]	HiViT-B [59]			0.0	5.6	0.0	0.0	15.2	13.0			5.4	0.0	22.3	2.1	0.0	2.6	5.4
S12-MoCo [43]	ViT-S [7]			0.0	4.3	0.0	0.0	17.4	15.1	7.4		0.6	0.0	<u>21.4</u>	0.8	0.0	10.3	5.5
S12-DINO [43]	ViT-S [7]			0.0	2.8	0.0	0.0	32.6	9.0	8.9		3.6	0.0	15.5	2.5	0.0	4.2	4.3
S12-MAE [43]	ViT-S [7]			0.0	3.0	0.0	0.0	<u>35.3</u>	22.0	12.1		1.5	0.0	21.2	0.9	0.0	8.7	5.4
DOFA [60]	ViT-B [7]			0.0	2.8	0.8	30.3	17.6	10.3			4.5	0.0	20.8	2.6	0.0	0.6	4.8
SatMAE [5]	ViT-L [7]			0.0	2.9	0.0	22.8	33.4	11.8			0.0	0.0	20.4	2.0	0.0	0.0	12.1
ScaleMAE [35]	ViT-L [7]			0.0	0.0	0.0	0.3	11.9	2.4			15.5	0.0	14.9	2.4	0.0	26.2	9.9
RemoteCLIP [26]	ViT-L [7]			0.0	3.3	0.0	34.0	25.7	<u>12.6</u>			18.0	0.0	20.5	0.0	0.0	0.0	6.4
MTP [44]	ViT-L [7]			0.0	0.2	0.0	1.8	11.0	2.6			0.3	0.0	21.1	2.0	0.0	0.0	3.9
DINOv2 [53]	ViT-L [7]			0.0	4.3	5.8	0.4	48.3	13.4			51.3	0.0	13.5	2.5	16.6	22.7	17.8
DINOv3 [42]	ViT-L [7]			0.0	<u>5.1</u>	0.1	41.7	51.3	15.7			20.8	0.0	1.7	2.5	0.0	36.4	15.3
CrossEarth-SAR-S	ViT-S [7]			0.0	4.6	11.4	14.2	65.6	14.1 (+0.7)			<u>49.7</u>	0.9	11.5	2.6	18.5	32.8	19.0 (+1.2)
CrossEarth-SAR-B	ViT-B [7]			0.7	4.3	<u>12.1</u>	1.6	<u>65.1</u>	<u>15.2</u> (+1.8)			49.1	0.0	15.6	2.6	14.0	38.9	20.0 (+2.2)
CrossEarth-SAR-L	ViT-L [7]			4.5	3.3	<u>7.2</u>	1.6	60.0	16.9 (+3.5)			42.6	0.0	10.8	2.5	<u>28.9</u>	<u>44.9</u>	23.7 (+5.9)
CrossEarth-SAR-L*	ViT-L [7]			<u>1.8</u>	3.2	16.3	6.3	54.2	<u>16.1</u> (+2.7)			33.1	<u>0.0</u>	17.9	2.6	31.5	46.5	<u>23.1</u> (+5.3)
SARATR-X [13]	HiViT-B [59]			15.8	22.6	6.2	28.4	27.4	21.3			10.8	0.0	5.4	0.0	5.9	4.2	4.4
S12-MoCo [43]	ViT-S [7]			16.2	11.4	0.2	20.9	24.6	14.7			17.9	2.2	<u>37.7</u>	0.0	0.0	27.8	8.1
S12-DINO [43]	ViT-S [7]			11.7	43.4	1.5	5.7	55.9	23.6			24.2	8.1	4.1	0.0	0.5	29.4	9.5
S12-MAE [43]	ViT-S [7]			12.4	10.1	0.7	20.1	13.6	11.4			12.0	1.7	39.9	0.0	0.0	10.4	8.8
DOFA [60]	ViT-B [7]			10.3	<u>46.6</u>	0.8	2.4	51.3	22.3			14.3	2.4	19.4	0.0	4.2	<u>32.8</u>	10.2
SatMAE [5]	ViT-L [7]			15.7	4.8	0.2	16.0	28.9	13.1			13.6	2.9	4.4	0.0	8.8	13.1	9.9
ScaleMAE [35]	ViT-L [7]			15.8	2.9	0.7	<u>20.9</u>	2.7	8.6			13.5	0.0	17.3	0.0	0.0	18.3	8.2
RemoteCLIP [26]	ViT-L [7]			10.0	42.8	1.0	11.2	43.0	21.6			11.7	0.6	32.5	0.0	0.0	19.4	10.7
MTP [44]	ViT-L [7]			1.9	53.1	0.2	11.6	43.4	22.0			6.2	3.5	6.7	0.0	0.0	10.0	4.1
DINOv2 [53]	ViT-L [7]			16.7	18.1	8.5	6.7	28.4	15.5			18.0	9.5	8.5	0.0	<u>7.1</u>	35.0	10.1
DINOv3 [42]	ViT-L [7]			11.2	30.9	6.0	13.6	57.9	23.9									8.8
CrossEarth-SAR-S	ViT-S [7]			<u>20.5</u>	3.2	<u>13.3</u>	15.7	<u>58.3</u>	21.3 (+5.8)			13.6	18.0	1.7	0.0	0.7	6.7	<u>10.7</u> (+0.6)
CrossEarth-SAR-B	ViT-B [7]			18.0	21.7	11.8	7.6	58.1	24.2 (+8.7)			27.8	3.56	10.4	0.0	4.6	16.0	9.4 (-0.7)
CrossEarth-SAR-L	ViT-L [7]			16.1	9.3	9.7	6.5	29.0	25.0 (+9.5)			19.9	2.2	14.7	<u>0.0</u>	6.2	16.8	9.6 (-0.5)
CrossEarth-SAR-L*	ViT-L [7]			20.9	13.5	13.7	14.9	71.9	27.0 (+11.5)			<u>27.4</u>	<u>10.0</u>	2.0	0.0	3.1	21.6	11.3 (+1.2)

Table 12 Performance comparison on benchmark for gaps3. **Bolds** = best; underlines = second best. Bldg:Buildings. Otr:Others. Veg:Vegetation. Wtr:Water. Farm:Farmland. Green:Greenery.

Method	Backbone	Domain		Classes					mIoU (%)	Domain		Classes					mIoU (%)	
		Source	→ Unseen	Bldg	Otr	Road	Veg	Wtr		Source	→ Unseen	Bldg	Farm	Green	Otr	Road		Wtr
SARATR-X [13]	HViT-B [59]			12.3	0.0	0.0	0.0	0.0	21.7			0.0	0.0	<u>23.0</u>	0.0	0.0	<u>50.4</u>	12.2
S12-MoCo [43]	VIT-S [7]			15.2	0.4	0.0	22.0	1.9	6.7			0.0	0.6	22.2	0.0	0.0	39.0	10.3
S12-DINO [43]	VIT-S [7]			18.9	19.4	0.0	25.5	13.6	15.5			7.4	11.8	20.3	0.0	0.0	41.7	13.6
S12-MAE [43]	VIT-S [7]			18.3	3.7	0.2	<u>27.1</u>	48.5	19.6			0.0	0.1	22.4	0.0	0.0	48.8	11.9
DOFA [60]	VIT-B [7]			15.8	4.9	0.1	13.6	7.0	8.3			0.0	0.0	22.5	0.0	0.0	51.5	12.3
SatMAE [5]	VIT-L [7]		D2F	6.9	43.9	3.7	0.0	0.0	20.3			0.8	0.0	0.0	0.0	0.0	11.9	10.2
ScaleMAE [35]	VIT-L [7]		(Unseen Region, Polarization and Microwave Band)	16.6	3.6	2.8	21.9	63.6	18.6			9.1	0.0	20.8	0.0	0.0	14.3	7.4
RemoteCLIP [26]	VIT-L [7]			18.5	0.6	0.0	27.3	62.3	21.7			1.2	0.0	21.9	0.0	0.0	30.0	8.9
MTP [44]	VIT-L [7]			15.5	18.0	0.1	7.7	6.5	7.1			46.2	0.1	6.9	0.2	0.6	21.4	12.5
DINOv2 [53]	VIT-L [7]			15.0	<u>42.9</u>	2.2	1.4	68.5	<u>26.0</u>			<u>48.5</u>	13.0	0.3	0.8	1.5	36.3	16.7
DINOv3 [42]	VIT-L [7]			17.7	15.3	0.0	7.1	0.8	22.1			0.0	0.0	26.1	0.0	0.0	26.5	13.7
CrossEarth-SAR-S	VIT-S [7]			<u>20.3</u>	24.9	3.2	4.0	58.5	22.6 (-3.4)			40.0	16.6	21.5	1.7	13.2	26.0	16.4 (-0.3)
CrossEarth-SAR-B	VIT-B [7]			19.3	11.5	6.8	3.0	<u>65.3</u>	21.2 (-4.8)			55.4	<u>24.6</u>	10.1	0.1	37.1	26.0	20.0 (+3.3)
CrossEarth-SAR-L	VIT-L [7]			20.4	30.9	<u>5.1</u>	5.0	55.4	25.1 (-0.9)			<u>67.7</u>	22.4	19.4	2.6	16.5	35.3	22.2 (+5.5)
CrossEarth-SAR-L*	VIT-L [7]			19.2	29.6	4.6	7.7	61.9	26.5 (+0.5)			67.8	30.8	6.2	<u>2.0</u>	<u>29.6</u>	37.5	25.6 (+8.9)
SARATR-X [13]	HViT-B [59]			0.0	23.2	1.6	0.3	49.7	15.0			10.3	0.0	0.0	0.0	0.0	5.7	2.7
S12-MoCo [43]	VIT-S [7]			0.2	16.5	0.0	18.8	51.4	17.4			11.7	6.8	12.8	0.0	0.0	0.0	5.2
S12-DINO [43]	VIT-S [7]			0.0	21.0	0.0	10.1	48.5	15.9			15.0	0.2	28.9	0.0	0.3	16.4	10.1
S12-MAE [43]	VIT-S [7]			0.0	15.1	0.0	16.0	49.2	16.1			11.5	44.2	11.7	0.0	0.0	21.1	14.8
DOFA [60]	VIT-B [7]			0.0	15.8	2.7	13.9	47.7	16.0			13.2	26.8	22.6	0.0	0.0	12.2	12.5
SatMAE [5]	VIT-L [7]		F2D	0.0	3.1	0.0	23.1	41.5	17.5			14.9	41.0	5.6	0.0	0.7	24.8	7.7
ScaleMAE [35]	VIT-L [7]		(Unseen Region, Polarization and Microwave Band)	0.0	23.2	0.2	6.4	51.4	16.3			10.0	0.0	6.5	0.0	0.5	14.7	5.3
RemoteCLIP [26]	VIT-L [7]			0.0	17.6	0.0	15.0	45.0	15.5			14.2	6.4	19.9	0.0	0.0	25.8	11.0
MTP [44]	VIT-L [7]			0.0	0.0	0.0	19.5	20.6	8.0			0.5	27.6	14.2	0.0	0.0	26.4	11.4
DINOv2 [53]	VIT-L [7]			7.2	<u>25.3</u>	<u>17.5</u>	0.2	<u>56.9</u>	<u>21.4</u>			10.3	38.3	1.8	0.0	0.3	<u>32.3</u>	13.8
DINOv3 [42]	VIT-L [7]			0.0	11.8	0.0	<u>21.3</u>	39.4	19.5			2.4	8.9	32.4	1.9	1.5	19.6	13.4
CrossEarth-SAR-S	VIT-S [7]			<u>9.0</u>	25.2	<u>22.7</u>	0.6	59.3	21.7 (+0.3)			15.8	37.3	29.9	0.0	3.3	34.0	18.9 (+5.1)
CrossEarth-SAR-B	VIT-B [7]			8.1	<u>25.4</u>	25.3	0.0	61.7	23.2 (+1.8)			<u>16.6</u>	33.8	8.1	0.0	0.3	29.4	15.3 (+1.5)
CrossEarth-SAR-L	VIT-L [7]			14.8	25.5	20.2	0.2	58.5	25.0 (+3.6)			21.8	<u>41.9</u>	37.1	0.0	<u>2.9</u>	30.0	18.0 (+4.2)
CrossEarth-SAR-L*	VIT-L [7]			1.7	25.2	18.6	0.6	<u>60.9</u>	<u>24.1 (+2.7)</u>			14.3	39.7	<u>36.2</u>	<u>0.1</u>	0.3	32.0	19.4 (+5.6)

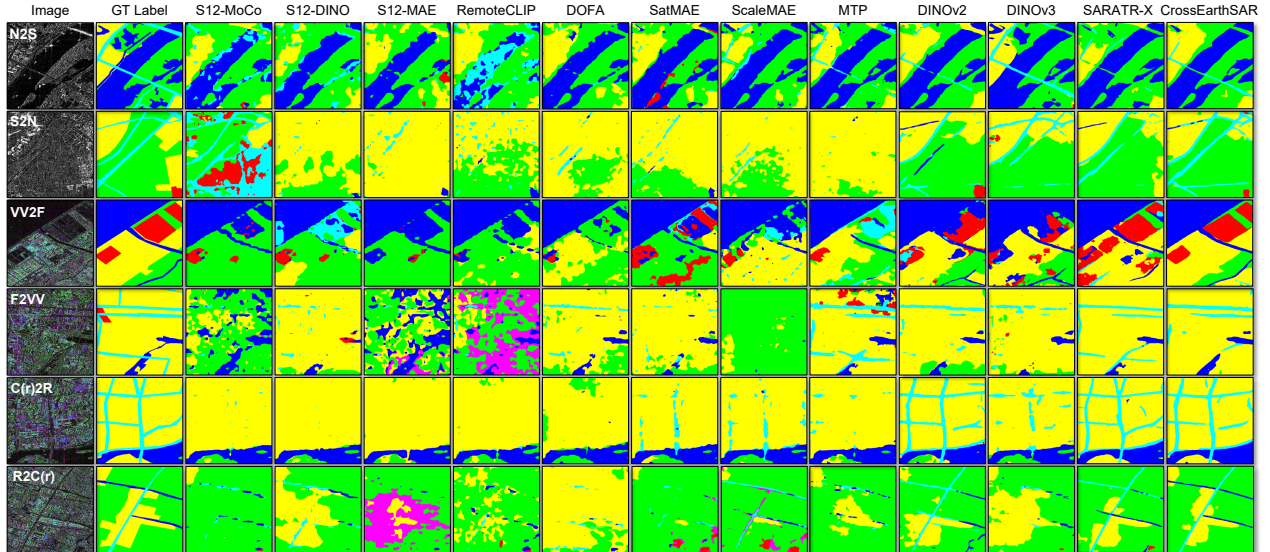


Figure 9 Visualizations of predicted segmentation maps on six representative benchmarks. The blue is the water class, green is the vegetation class, red is the ground class, cyan is the road class, yellow is the building class, and purple is the mountain class.

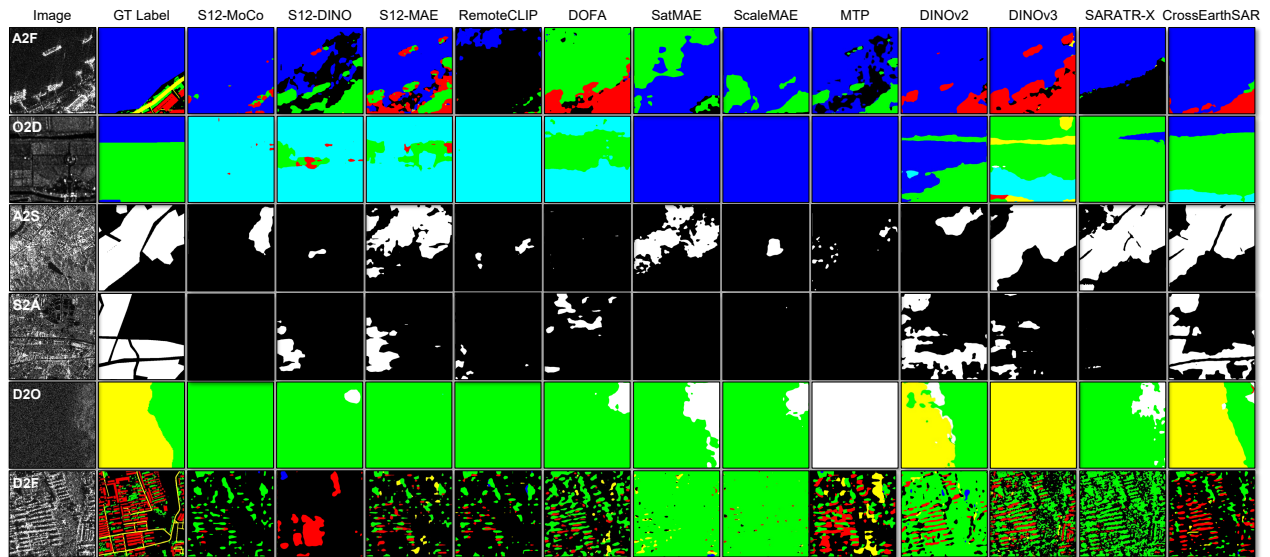


Figure 10 Visualizations of predicted segmentation maps on six representative benchmarks. The **blue** is the farmland class, **green** is the greenery class, **red** is the road class, **cyan** is the building class, **yellow** is the water class, and white is the background class.

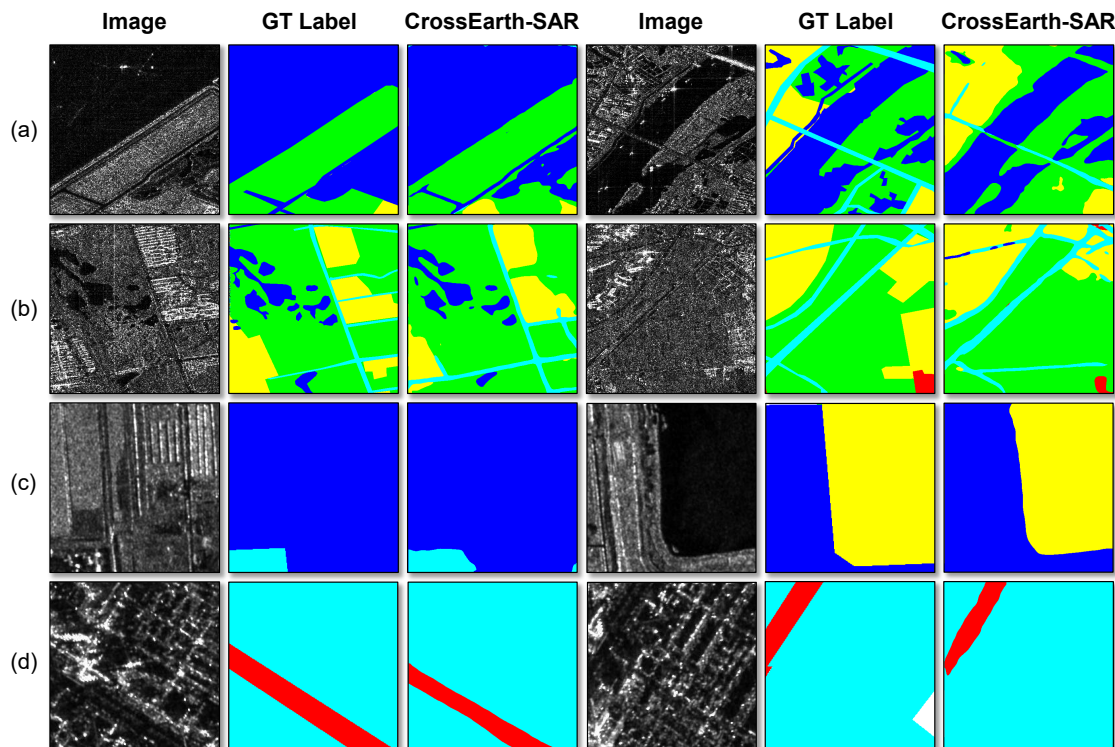


Figure 11 Visualizations of predicted segmentation maps on 1-4 benchmarks. Images in (a) and (b) respectively represent N2S and S2N. The **blue** is the water class, **green** is the vegetation class, **red** is the ground class, **cyan** is the road class, **yellow** is the building class, and **purple** is the mountain class. Images in (c) and (d) respectively represent K2C and C2K. The **blue** is the farmland class, **green** is the greenery class, **red** is the road class, **cyan** is the building class, **yellow** is the water class, and white is the background class.

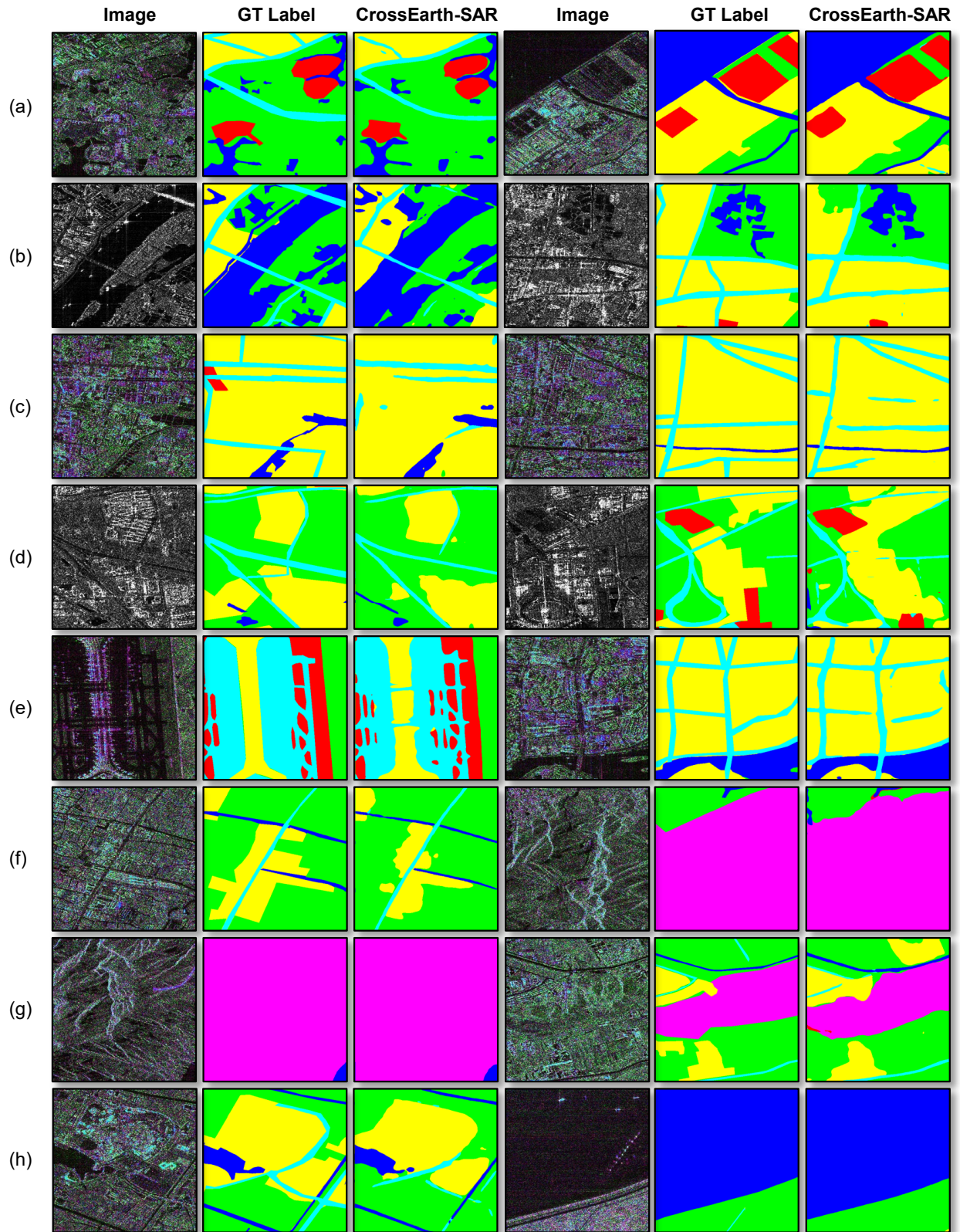


Figure 12 Visualizations of predicted segmentation maps on 5-12 benchmarks. Images in (a), (b), (c), and (d) respectively represent VV2F, F2VV, HH2F, F2HH. Images in (e), (f), (g), and (h) respectively represent C(r)2R, R2C(r), C(i)2R and R2C(i). The blue is the water class, green is the vegetation class, red is the ground class, cyan is the road class, yellow is the building class, and purple is the mountain class.

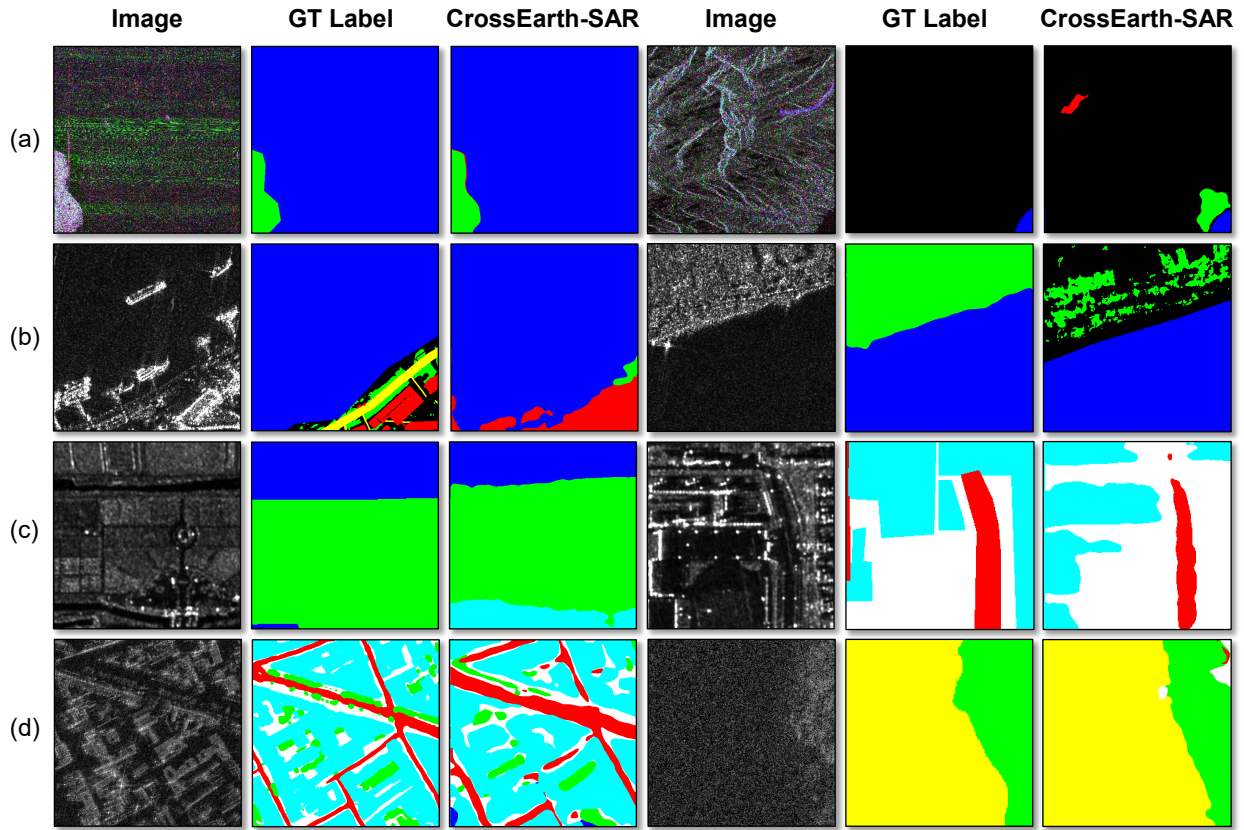


Figure 13 Visualizations of predicted segmentation maps on 13-16 benchmarks. Images in (a) and (b) respectively represent F2A, A2F. The blue is the water class, green is the vegetation class, red is the building class, yellow is the road class, and black is the other class. Images in (c) and (d) respectively represent O2D, D2O. The blue is the farmland class, green is the greenery class, red is the road class, cyan is the building class, yellow is the water class, and white is the background class.

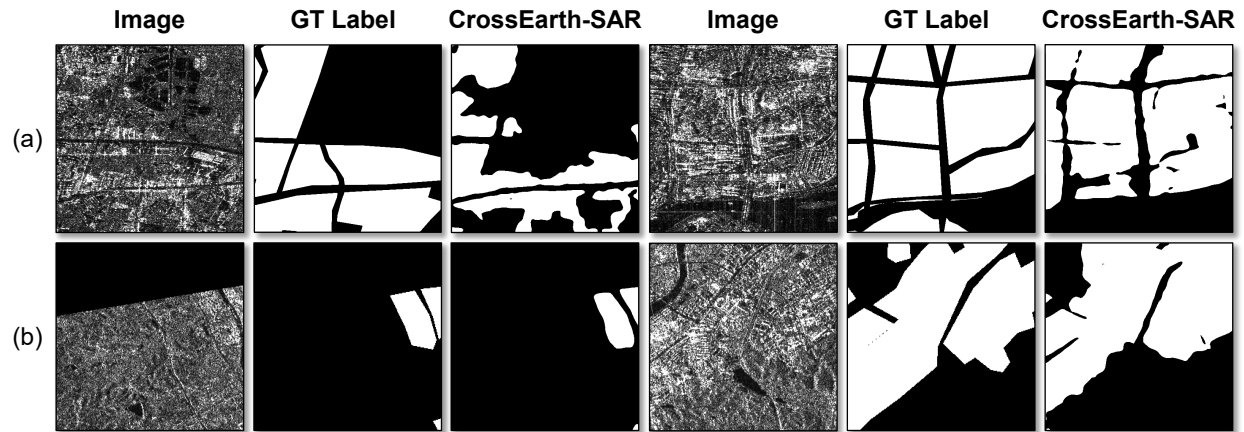


Figure 14 Visualizations of predicted segmentation maps on 17-18 benchmarks. Images in (a) and (b) respectively represent S2A and A2S. The white is the building class, black is the other class.

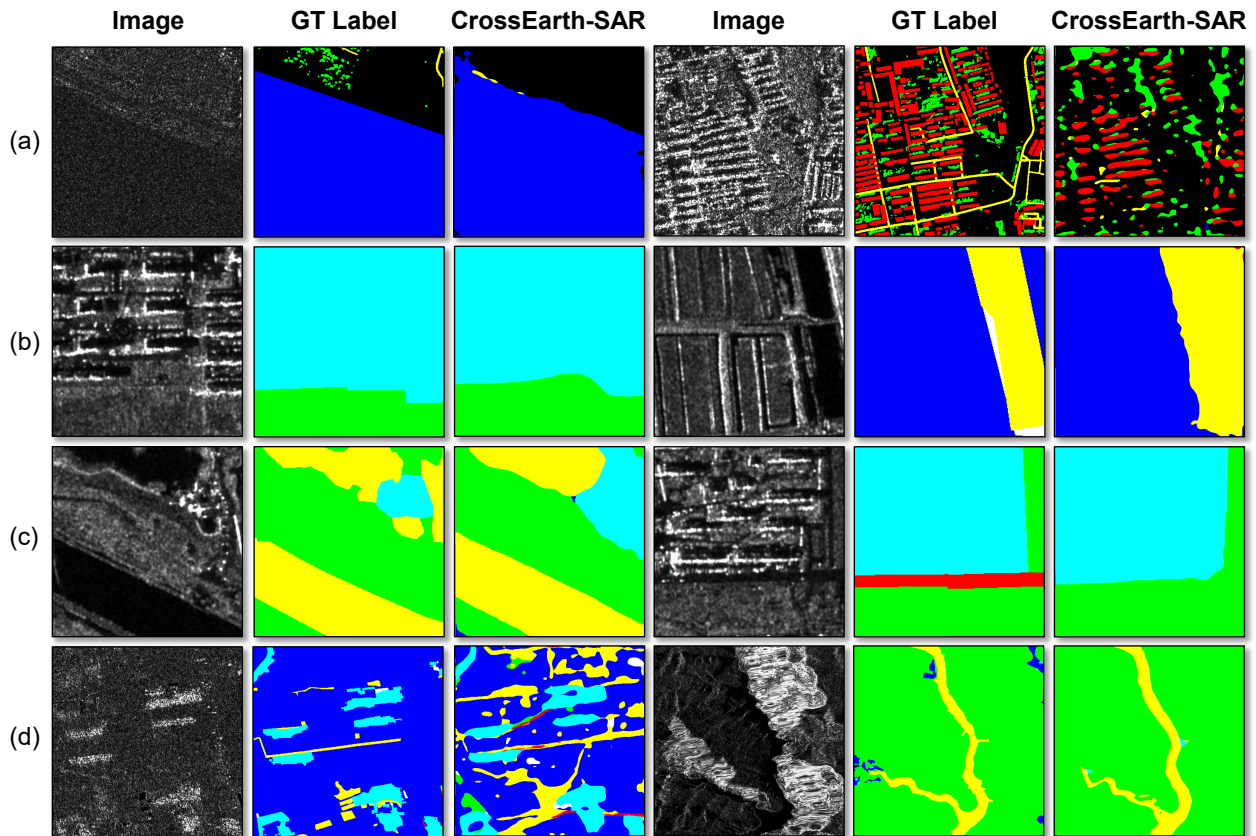


Figure 15 Visualizations of predicted segmentation maps on 19-22 benchmarks. Images in (a), (b), (c), and (d) respectively represent D2F, F2D, W2D and D2W. For the D2F benchmark, the blue is the water class, green is the vegetation class, red is the building class, yellow is the road class, and black is the other class. For the other three benchmarks, the blue is the farmland class, green is the greenery class, red is the road class, cyan is the building class, yellow is the water class, and white is the background class.